We are IntechOpen, the world's leading publisher of Open Access books
Built by scientists, for scientists

6,900
Open access books available

185,000
International authors and editors

200M
Downloads

Our authors are among the

154
Countries delivered to

TOP 1%
most cited scientists

12.2%
Contributors from top 500 universities

CLARIVATE ANALYTICS
BOOK CITATION INDEX
INDEXED

WEB OF SCIENCE™

Selection of our books indexed in the Book Citation Index
in Web of Science™ Core Collection (BKCI)

Interested in publishing with us?
Contact book.department@intechopen.com

Numbers displayed above are based on latest data collected.
For more information visit www.intechopen.com

Chapter

Polyimide: From Radiation-Induced Degradation Stability to Flat, Flexible Devices

Prashant S. Alegaonkar, Vasant N. Bhoraskar and Sudha V. Bhoraskar

Abstract

Polyimide (PI, PMDA-ODA, $C_{22}H_{11}N_2O_5$, Kapton-H), is a class of polymer, extensively used in microelectronics and space technology, due to its exceptional mechanical, dielectric, and chemical properties. In space, PI heat shield experiences a harsh environment of energetic electrons, ultra-violet radiation, and atomic oxygen, causing degradation and erosion. Radiation-assisted physicochemical surface modulations in PI, in view of understanding and reducing the degradation in laboratory-based systems, are discussed in the chapter. Strategies for the design and development of 2D, flat, and flexible electromechanical devices by swift heavy ion induced bulk modifications in PI are also described. Fabrication of a couple of such devices, including their performance analysis, is presented.

Keywords: polyimide, radiation, degradation, stability, devices

1. Introduction

As one of the high-performance polymers, aromatic polyimides (PIs), find applications in many high-tech fields due to their excellent thermal and oxidative stabilities, high mechanical strength, flexibility, and good dielectric properties. Its importance has been established on the basis of exceptional and versatile properties, which is unparallel to most other classes of macromolecules. There are both thermosetting and thermoplastic PIs. In fact, there are many published comprehensive works on PIs' chemistry, synthesis, characterization, and applications [1–3]. PIs were first synthesized by chemists at Dupont in the 1950s and are popular by the trade name of Kapton. Most often, this aromatic form of PI is used for space applications. Kapton is prepared through condensation polymerization of pyromellitic dianhydride (PMDA) and oxy-di-aniline (ODA).

PIs are used extensively in aerospace, gas separation, memory devices, and in the microelectronics industry. PI also finds application in the electrical industry as insulation coating of electromagnetic wirings. It can withstand the temperature of 425°C for short time exposures without undergoing any degradation or deformation. For this reason, PI finds application in supersonic aircraft and in space vehicles. Most of the materials developed for the space application were initiated during

the 1960s, when Sputnik—"Satellite I" was launched by the Soviet Union. Then onwards space programs were developed in various directions. The applications involved the requirements in various earth orbits and interplanetary missions. Earth orbits are classified as low Earth orbit (LEO), between 200 and 800 km, geostationary Earth orbit (GEO) defined at 36,000 km above the equator, and medium Earth orbit (MEO), existing between LEO and GEO. Each orbit is employed for specific applications, like navigation, communication, and for use in Earth observation satellites.

However, prolonged use of spacecraft materials and their exposure to the space environment leads to the degradation of thermal, electrical, mechanical, and optical properties, which can subsequently result in an early mission failure. Materials used in space are exposed to various hazards, which include ultraviolet (UV) radiations and other ionizing radiations (like energetic electrons, protons, and heavy ions) [4]. Ground-simulated research is, therefore, extensively required to safeguard the properties of PI from these radiations [5].

Further, due to the developments in micro and nanoelectronics which are approaching smaller and smaller sizes at increasing production costs, many small- and medium-sized manufacturers have realized the difficulty of survival due to the harsh competition. Here polymeric electronics offers the solution with flexible thin-printed transistor electronics which can provide large-size displays. These nanosized structures are capable of covering the bridge between the "classical" silicon-based, and the new polymer-based electronics. One such development is based on the ion tracks in polymers: similar to those formed in photoresist and SiO_2 (both of which are the vital components of many silicon-based structures). Now silicon/track hybrid structures may be designed inside the polymers. These ion tracks in polymer foils will form a multitude of new interesting applications not only in electronics but also in other fields such as medicine or optics.

Ion tracks [6] are formed in polymers when high-energy ions damage the polymer by the process of chain scission and cross-linking along their passage. As a result of bond breaking in the polymer, gases like hydrogen, CO_2, CO, or CH_4 are liberated along the trajectory. When these gases get emitted out of the surface, they create holes and thus form the tracks which are often called Latent Tracks. After chemical etching and removing the damaged matter using a suitable etchant, these tracks get opened up. They are visible with a microscope and are called Etched Ion Tracks [6]. If such tracks are filled with an appropriate material like silver or gold, they can generate nanowires or nanorods within the polymer [7]. By generating such structures in PI and filling the tracks with silver, Fink et al. [6] have successfully fabricated micro-transformers. Petrov et al. [8] have reported on the effects of time of irradiation on the crystallinity, conductivity, and wall thickness of the nanotubes [8].

The use of PI in electronic applications is also exhibited by its good electrical and dielectric stability, apart from its mechanical strength. In general, polymers are low dielectric constant ($\acute{e}$) materials. Polyimide for example has a dielectric constant equal to ~3.15. Inorganic materials and oxides have relatively higher values of dielectric constant (between 4 and 9). The values of the dielectric constant can be therefore tailored by making composites or by doping an external material into the host polymer. To find suitable applications as an insulator, the material should preferably have a low dielectric constant. In fact, both, the dielectric constant and dielectric relaxation (τ) are especially important in deciding the suitability of the polymer in technological applications. These properties are controlled to some extent by the defects and space-charge, generated, within the folded chains of a polymer. Defects generated during the synthesis also lead to the formation of dipoles within the polymer matrix and they control the dielectric properties. This

results in the dielectric-relaxation described by the value of dissipation factor, tan δ, and its relation with τ_0 (the relaxation time for dipole orientation) given by the expression [9, 10]:

$$\tan \delta = 2\,\pi f.\tau_0.S_r / 1 + (2\,\pi f\,\tau_0)^2. \tag{1}$$

Here, S_r is the relaxation strength which depends on the number density of the dipoles and f is the frequency of the applied electric field.

Due to its high mechanical and thermal stability PI is used as an excellent dielectric material for spacecraft technologies. There are reports [11] whereby using the nano-foam morphology the dielectric constant of PI has been lowered from 3.2 to 2.5 at ambient temperatures, and from 2.9 to 2.3 at 100°C. On the other hand, there are reports [12] where the refractive index (directly related to the dielectric constant) has been increased in fluorinated PI when it is irradiated with 25 keV electrons at a fluence of ~5 × 10^{15} e/cm^2. The dielectric constant is also very influential in controlling the signal transmission and its attenuation when PI is used for packaging in high-speed microelectronic devices [13]. High values of the dielectric constant are useful when the polymers are used as insulating layers in the high voltage capacitors. Such studies have been, therefore, carried out with PI from the point of view of finding its applications in the micro-electronic and optoelectronic fields [14–17]. However, the bulk resistivity of a polymer should be as high as possible to protect its insulating characteristics. These are often the fundamental issues that are aimed at while tailoring the dielectric properties of polymers.

Again, while talking about the space applications of PI its interaction with high energy ionizing radiations becomes quite imperative. Effect of ionizing radiations on polymers, radiation processing of polymers, surface modifications, and use of radiations for nanotechnology [18–22] have been largely reported. In general, the irradiation on polymer leads to the formation of reactive species such as free radicals.

PI is used as a shielding material in different application areas. These include space missions, automotive industries, and nuclear electronics. In these applications, its optical reflectivity also plays an important role. It is also used as a thermally strong insulator in several electronic circuits [23, 24]. There are reports where its thermal and mechanical properties are studied as a function of high energy radiations such as 3 MeV protons [24] and 2 MeV electron irradiation [25]. Effects of 2 MeV electron irradiation have been reported to alter the mechanical properties of PI [26]. The change in the hardness and Youngs Modulus by 4 MeV light ions on different kinds of PIs are also reported [27]. Radiation processing using high-energy electron irradiation is especially preferred for polymers because of their high dose rates and high-energy deposition in lesser time intervals. High processing rates are achieved because a high dose rate also initiates a high rate of cross-linking as oxidation effects are relatively weak at the high dose rates. Moreover, electron irradiation facilities are easily controllable and one can achieve steady dose rates without any interruption of homogeneous energy deposition [28, 29]. In particular, the effects of high-energy pulsed electron irradiation for studying the surface processing of PI need more attention.

In satellites, PI is used for different applications such as shielding material for thermal control, insulating material in electronic circuits, and similar others. The satellites that are designed to operate in the low Earth orbits region (LEO) [30, 31] are exposed to atomic oxygen in addition to other space radiations such as electrons, protons, and UV radiation [32–34]. As the period of exposure to this radiation increases, the physicochemical, mechanical, optical, thermal, and electrical properties of polymers degrade at a faster rate [32]. Effects of Atomic Oxygen (AO)

having energies between 5 and 20 eV carries significant importance since the space shuttle in the LEO region is exposed to such atomic oxygen species.

In space, the AO is generated when the short-wavelength ultraviolet radiation (>5.12 eV, <243 nm) dissociates molecular oxygen present in the upper atmosphere [33–35]. The space vehicle normally moves with a velocity of 7–8 km s^{-1} in the LEO region. The energy of the atoms of oxygen is decided by the velocity of the space vehicle. The energy with which the atoms of the oxygen impinge on the spacecraft surface, moving with a high velocity, becomes around 5 eV. In this LEO region, the flux of the atomic oxygen varies from ~10^{12} to 10^{15} atoms cm^{-2} s^{-1} [36]. The surface region of the polymer which is used as a shielding material over the space-craft, therefore, receives fluences of ~10^{19}–10^{22} ions cm^{-2} in a period of about 1 year. During the mission period of the spacecraft in the LEO region, the deteriora-tion observed on the surface of the polymer is therefore mainly correlated to the irradiation effects of the atomic oxygen [37]. The polymer-like PI which is used as a shielding material then gets eroded and loses its weight. The rate of weight loss depends on the flux of the atomic oxygen. In general, the weight loss increases with increasing irradiation period [38–42].

In addition, at Low Earth Orbit, oriented spacecraft experiences asymmetric fluxes because of the interactions between the radiations with the environment. As a result, prior to the exposure to atomic oxygen, the spacecraft comes across other space radiations such as electrons, protons, and UV radiations [43–46]. The shielding material on the spacecraft then interacts with all these radiations during its passage which may be more detrimental for the polymer surface. With increasing time of interaction all the physicochemical and related properties of the polymers degrade at a faster rate [47]. Ionizing radiations produce defects mainly by cross-linkages and chain scission. These processes are assisted by bond breakages or weakening of the bonds resulting in the emission of gaseous species from the surface. Moreover, atomic oxygen is very reactive due to the lone pair of electrons it has. Several interactions can occur over the polymeric surface, such as oxidative reactions with surface atoms or adsorbed molecules, both elastic as well as inelastic scattering recombination, associ-ation, or excitation of species. Atomic oxygen can very strongly react chemically with a surface and cause the formation of volatile oxides from polymers. The surface layer gets eroded. Although PI is a thermally stable polymer it is also seen to get degraded by AO. As a consequence of such degradation, research in this area still remains one of the hot topics with PI. The erosion yield of the polymer is also influenced by other physical parameters like the impact angle, temperature, flux, and total fluence of atomic oxygen, synergistic effects of other radiations, and the energy during the impact of the atomic oxygen [48, 49].

There is no dearth of literature where the effect of one kind of radiation alone has been investigated on the change in the properties of PI. For example, Hill et al. have studied the effects of 3MeV proton radiation on the mechanical properties [24], Plis et al. have investigated the spectroscopic and thermal properties of 2MeV electron irradiation [50], Sasuga et al. report the effect of 2MeV electron radiation on the mechanical properties [26] and Cherkashina et al. have studied the effect of 4MeV light ions on the hardness and Youngs' modulus [51] of various polyamides. In our earlier publication [52] it has been shown that 1 MeV pulsed electron beam can be used to simulate conditions similar to space radiations. The surface and bulk proper-ties of PI were modified to investigate the role of electron fluence. Our group has also reported [53–55] the erosion properties of PI and studied the rate of weight loss as a function of the flux of atomic oxygen generated in Electron Cyclotron Plasma. Recently we have investigated the synergetic effects of electron irradiation on the surface erosion properties of PI by AO. The samples were irradiated with 1 MeV electrons prior to exposing them to the atomic oxygen. The electrons having fluence,

ranging from 5×10^{14} to 20×10^{14} electrons/cm^2, were obtained from the electron accelerator whereas, the atomic oxygen was generated in a plasma system. Post-characterization of the irradiated samples, using weight loss measurements, indicated that the extent of erosion by oxygen ions increases if the sample is pre-irradiated with 1 MeV electrons [42]. The paper also reports a larger extent of degradation in the optical transparency when samples were pre-irradiated by electrons.

The chapter highlights the effects of radiations (electrons and gamma radiations) in multiple ways. It is used in modifying the dielectric properties and also for elemental doping by radiation-enhanced diffusion process. The surface erosion properties by atomic oxygen, obtained by a ground-based electron cyclotron resonance plasma simulator are also discussed. The use of swift heavy ions in fabricating the micro-electronic device is also presented. The results of different experiments carried out with PI are sequentially described in separate sections.

2. Effect of 1-MeV electron irradiation on dielectric function: boron and fluorine diffusion

Studies related to the dielectric measurements have been extensively carried out in our group and are reported in our earlier communication [53] (Alegaonkar APL 2002). Here, we have chosen a polyimide ($C_{22}H_{10}N_2O_5$, PMDA-ODA, Kapton-H) sheet having a thickness of ~50 mm. The electron irradiation was carried out with a microtron accelerator which was used in the pulsed mode of operation by varying the electron fluence over the range of 10^{14}– 10^{15} e/cm^2. The weight loss of the PI samples after electron irradiation, having dimensions of 12 mm × 12 mm, was monitored. All the electron-irradiated samples were subjected to dielectric relaxation measurements over a frequency range of 100 Hz–7 MHz. The values of dielectric constant έ, and the dielectric loss ĕ, were also estimated at each frequency by using the measured values of the capacitance and tan δ. Apart from this the value of the refractive index has been monitored at a wavelength of 622.8 nm, by using an ellipsometer.

The paper also discusses the effect of boron diffusion on the dielectric properties of the polyimide films and compares the effects with those of electron irradiated films. Gamma irradiation from Co-60 with a dose rate in the range from 6 to 48 Mrad was used in the process of radiation-assisted diffusion using BF_3 solution. The depth distribution of boron inside the film was studied using the technique of neutron depth profiling [56] and the presence of fluorine was confirmed by X-ray photoelectron spectroscopic measurements. Moreover, it was revealed that boron and fluorine had diffused from both the surfaces up to a depth of ~2 μm on account of gamma irradiation.

The paper reported that the frequency distribution of dielectric loss, ĕ, and the dielectric constant, ě, were influenced by the fluence of irradiation Φ. The measured refractive index has also been shown to depend on the electron fluence. The graphical representation of these parameters is shown in **Figure 1** (reproduced with permission Alegaonkar et al. [53]). The paper also highlights a small shift in the second peak in **Figure 1(a)** towards lower frequency and correlates it to an increase in the relaxation period with increasing electron fluence. This is governed by the relation: $\omega \bullet \tau_0 \bullet T \sim 1$ [1, 57]. The loss factor actually depends on the conductivity of the material. The electrical conductivity in PI, as in most of the polymers, is governed mostly by the mechanism of hopping of charge carriers from one defective site into another. Since electron irradiation is associated with the generation of defect sites it is influenced by the fluence of irradiation. Effectively the number of electrons that can undergo transition has increased with increasing electron fluence. As a result, the dielectric loss, έ, which is associated with electron transition, also
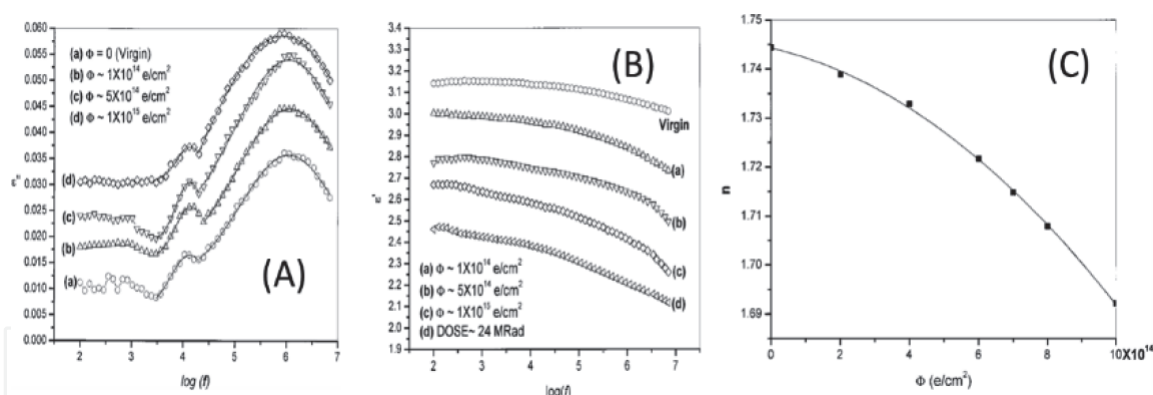
Figure 1.
*(A) Variations in dielectric loss, ě, with log(f) for PI samples irradiated with 1 MeV electrons at different fluences, Φ. (B) Variations in dielectric constant, ě, with log (f) for PI samples irradiated with 1 MeV electrons at different fluences, Φ [plots (a)–(c)] and for a PI sample immersed in BF₃ solution and irradiated with Co-60 gamma rays [plot (d)]. (C) For 1 MeV electron-irradiated PI samples, variation in refractive index, n, with electron fluence, Φ. Reproduced with permission from Alegaonkar et al. [53].*

increases with increasing electron fluence. Here, the dielectric constant, ($\acute{e}$ = 3.15) of virgin PI is reported to be independent of frequency, whereas for the electron irradiated PI it is seen to decrease as the frequency of the applied electric field increases. The lowest value of the dielectric constant is reported to be 2.4 (at ~7 MHz). For the boron-and-fluorine doped PI, the lowest value is seen to be 2.1 (at ~7 MHz). The refractive index, (η = 1.7444) of virgin PI has also been reported to decrease with electron fluence reaching the lowest value of ~1.6921, at an electron fluence of 1×10^{15} e/cm². The lowering of the dielectric constant has been correlated to the formation of **π**-electron clouds resulting from chain scission and cross-linking of molecular chains [2, 6, 7]. The polarization is aligned in the direction of the molecular chains. As a consequence, the refractive index in a direction perpendicular to the plane of the sample is also affected.

The paper also reports a measurable weight loss arising from the emission of gases such as oxygen, hydrogen, etc., from the PI matrix during irradiation. Thus, in this case, the density of the PI has been shown to decrease with increasing electron fluence. The result has been reproduced in **Figure 2**. It shows that the percentage of weight loss, W_L, increases with increasing electron fluence.
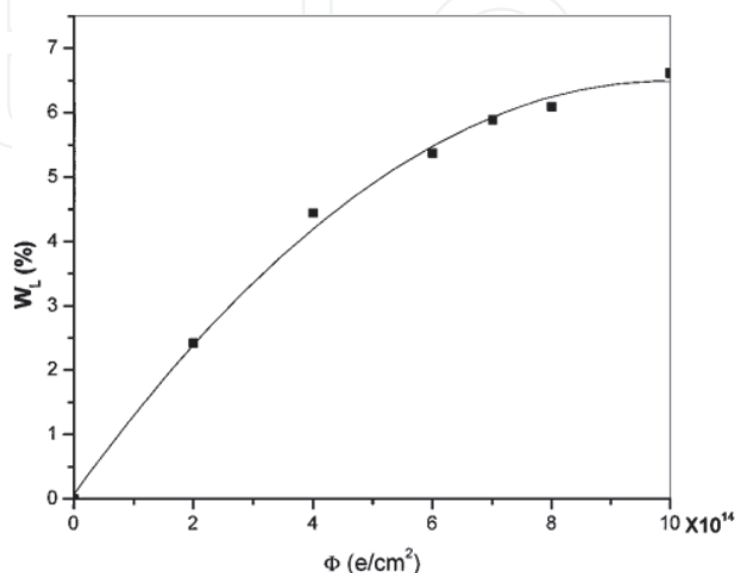
Figure 2.
For 1 MeV electron-irradiated PI samples, variation in weight loss, W_L (%), with electron fluence, Φ. Reproduced with permission. (Reproduced from Alegaonkar et al. [53]) ©Copy right 2002, Applied Physics Letters.

Apart from the irradiation with electrons, our group has also studied [58] the influence of doping the PI with boron and fluorine as stated in the earlier paragraph. Even though boron and fluorine were diffused up to a depth of ~2μm from each side, they lowered the dielectric constant of ~50 μm thick PI quite effectively. The variations in the dielectric constant, $\acute{\epsilon}$, and dielectric loss $\breve{\epsilon}$, with frequency, were almost similar to those irradiated with 1 MeV electrons at a fluence of 10^{15} e/cm^2. These results are important in view of finding the application of 50-μm thick PI, where lower values of dielectric constant are preferred.

In another report from our group [59] phosphorus, boron, and fluorine were doped into the PI films by the radiation-assisted diffusion. The dielectric constant, $\acute{\epsilon}$, of the PI, was again tailored over a small range around the value of 3.15.

3. Dielectric parameters of phosphorus and fluorine diffused PIs

Similar to the work which has been discussed in the previous section relating to the diffusion of boron into the surface layer of PI, we have also carried out investigations by doping phosphorous and compared the results with those obtained by doping with boron. The results have been reported in our earlier communication [59]. 50 μm thick PI samples of 15 mm × 15 mm were doped with phosphorous and fluorine by using the technique of radiation-assisted diffusion process. Solutions of H_3PO_4 and BF_3 were used to diffuse the elements of phosphorous and B/F into the matrix of PI. The doped samples were designated as S_P, in the case of P doping and $S_{B/F}$ in the case of boron and fluorine doping. Similarly, the unirradiated virgin PI samples are designated as S_V. Different doses of gamma rays, ranging from 64 kGy to 384 kGy from Co-60 were used as the source of radiations.

X-ray photoelectron spectroscopy (XPS) was used to confirm the presence of phosphorus in S_P and fluorine in $S_{B/F}$. The atomic concentrations (%) found from these measurements were as shown in **Table 1**. The paper describes the experimental results of the Rutherford Backscattering Technique which provided the depth of the diffusion of the phosphorus and fluorine in the PI samples. The RBS spectra for the S_P and the $S_{B/F}$ samples are as shown in **Figure 3(a)** and **(b)**, respectively. The RBS spectrum was deconvoluted and the elements present in the PI surface were identified. The average depth of diffusion of phosphorus or fluorine atoms in the PI, estimated at ~10% concentration relative to the peak concentration at the surface, was ~3 μm.

The reported RBS spectra have indicated the presence of phosphorus and fluorine as has been reproduced in **Figure 3**. The area under the RBS peaks has been shown to be proportional to the number of phosphorus or fluorine atoms diffused in

Dose of gamma-rays dose (kGy)	Atomic percentage (%)	
	Phosphorus	Fluorine
64	0.7	1.05
96	1.12	1.68
128	1.5	2.22
192	1.82	2.66
288	2.03	2.92
384	2.21	3.12

Table 1.
The atomic percentage of phosphorus in S_P and fluorine in $S_{B/F}$ samples for different doses of Co-60 gamma-rays, as estimated from the EDAX measurements.

Dose of gamma-rays dose (kGy)	Atomic percentage (%)	
	Phosphorus	Fluorine
64	0.7	1.05
96	1.12	1.68
128	1.5	2.22
192	1.82	2.66
288	2.03	2.92
384	2.21	3.12
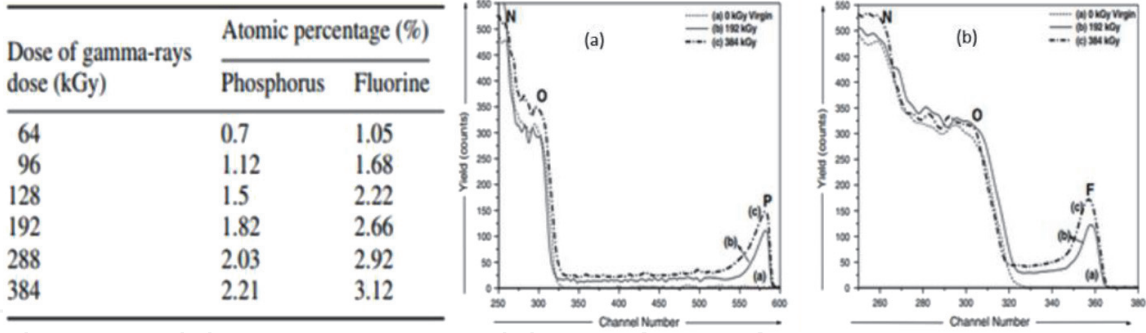
Figure 3.
(a) and (b) RBS spectra of the PI samples which were immersed in H_3PO_4 solution and BF_3 solution respectively. The samples were irradiated with Co-60 gamma-rays at a dose (a) 0 kGy; virgin, (b) 192 kGy and (c) 384 kGy. (Reproduced from [58]) Reproduced with permission ©Copy right 2006, Journal of Physics D.

the PI sample. In addition, the concentration of phosphorus or fluorine (relative %) is shown to increase with an increasing dose of Co-60 gamma-rays. From the results of the EDAX measurements shown in **Table 1**, Riyadh et al. [58] have reported that the atomic percentage of phosphorus, as well as that of fluorine, has increased with the dose of Co-60 gamma-rays. The results have been discussed in view of the defects induced in PI as an effect of gamma irradiation, which includes vacancies, cross-linking and bending of bonds, and formation of voids due to the diffusion of gaseous molecules [13]. The gases such as H, O, and C are normally evolved as an effect of radiolysis. The process of diffusion of external atoms into polymer surface is normally explained using the model based on free volume [58, 59].

Here, the depth of diffusion of the phosphorus and fluorine atoms is reported to be ~3μm. The authors [58] have further analyzed the results with the XPS spectrum (not shown here). The analysis is reported to have further indicated that phosphorus and boron atoms have formed bonds with oxygen atoms [60] in PI, whereas fluorine atoms have formed bonds with the carbon atoms [61] in the surface region. Here, the concentration, Cs, of the phosphorus and fluorine (Cs in relative %) in the S_P and $S_{B/F}$ samples have been obtained after normalizing the intensity of each XPS peak with respect to the corresponding photoelectric cross-section. The variations in the phosphorus and fluorine concentrations with the dose of Co-60 gamma-rays were determined which are represented in **Figure 4(a)** [62].

The dielectric constant, $\acute{\epsilon}$, estimated over the frequency range 100 Hz–7 MHz. are shown in **Figure 4(b)**. The spatial distribution of boron was studied with the
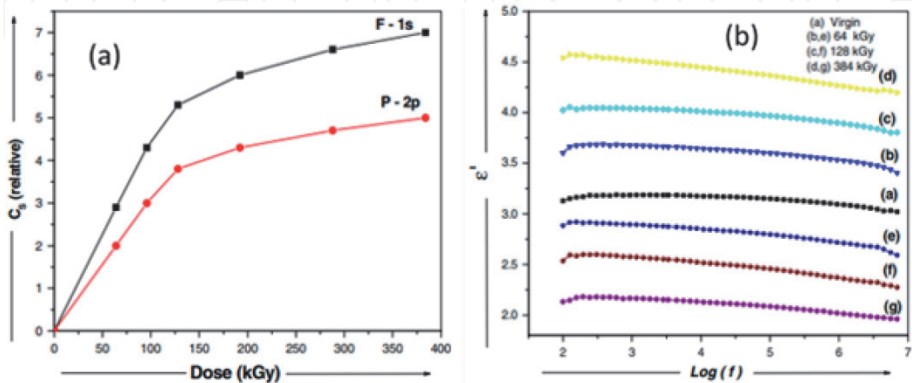
Figure 4.
Variations in the relative concentrations of phosphorus and fluorine with the dose of Co-60 gamma-rays. Variations in the dielectric constant, $\acute{\epsilon}$, with frequency, f, for the PI samples doped with phosphorus, boron, and fluorine at different doses of Co-60 gamma-rays over the range ~64–384 kGy; (i) virgin (a), (ii) phosphorus-doped (b), (c) and (d) and (iii) fluorine and boron-doped (e), (f) and (g). Reproduced with permission [2006] ©Copy right 2002, Nuclear Instruments and Methods–B. (Reproduced from [58]).
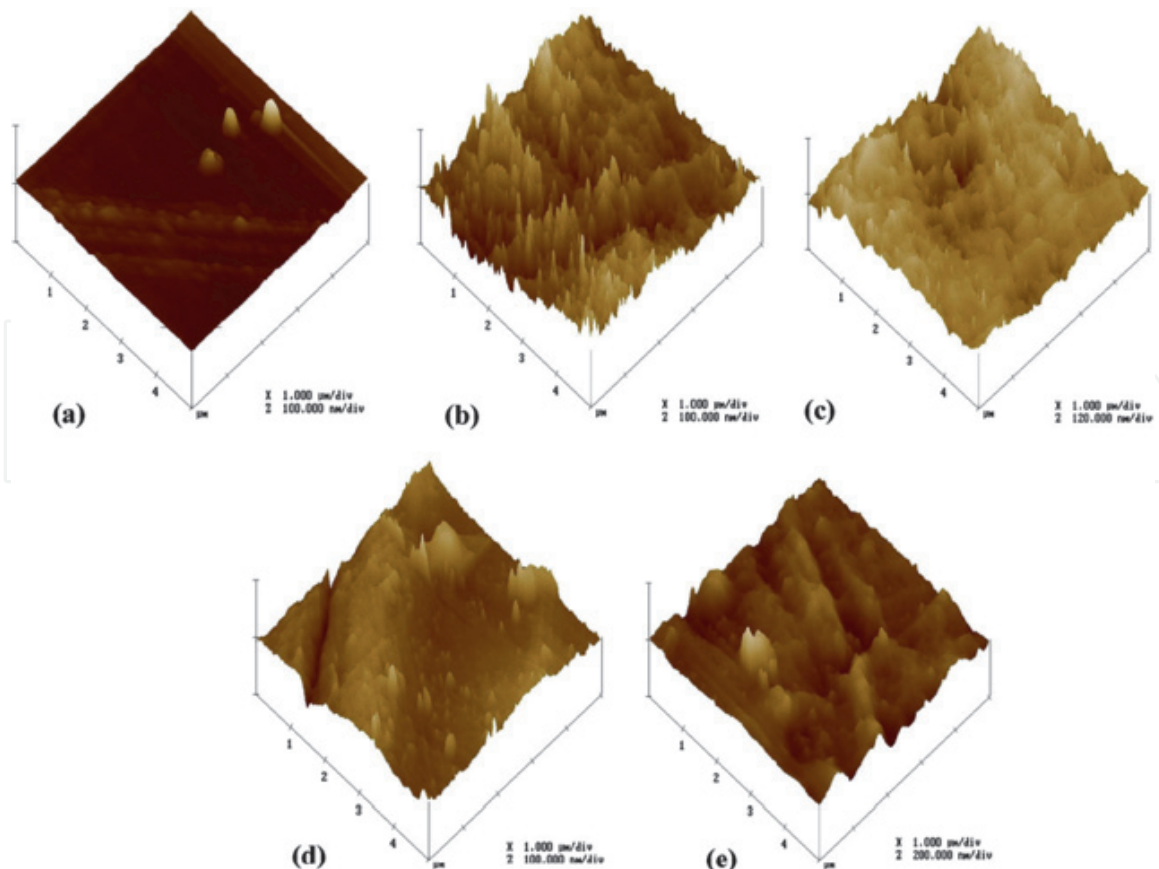
Figure 5.
AFM photographs showing surface images of the PI samples (i) (a) virgin, (ii) doped with phosphorus at gamma-ray dose of (b) 64 kGy, (c) 384 kGy and (iii) doped with boron and fluorine at gamma-ray dose of (d) 64 kGy, (e) 384 kGy. Reproduced with permission [59] © Copyright 2006, J. of Phys. D. [Reproduced from [59]].

neutron depth profiling technique using the nuclear reaction for ^{11}B (n, α) ^{7}Li. The experimental method was similar to that reported earlier for HDPE [57, 58].

The paper (reproduced from [58]) also reports the surface morphology using the atomic force microscope technique, in the non-contact mode. A few typical recorded surface images are reproduced in **Figure 5**. The micrograph (a) is for virgin S_V, and the micrographs (b) and (c) are for the S_P samples and (d) and (e) are for the $S_{B/F}$ samples.

The AFM images reproduced in **Figure 5**, are indicative of the change in surface morphology of PI as a result of doping with phosphorus, boron, and fluorine The RMS values of the surface roughness as reported for the S_V, S_P, and $S_{B/F}$ samples were 8.1 nm, 10.4 nm, and 16.7 nm respectively. As compared with the virgin, the surface roughness of the PI is reported to increase marginally after phosphorus doping but significantly after boron and fluorine doping. The authors have found that the mechanical properties of phosphorus, boron, and fluorine diffused PI were almost similar to those of the virgin PI.

The paper also reports the discussion on the variation of the dielectric constant $\acute{\epsilon}$, the density, ρ, and the polarizability, α, which are related [63] through the relation:

$$\left(\frac{\acute{\epsilon} - 1}{\acute{\epsilon} + 2}\right) \frac{M_w}{\rho} = \frac{N_A \, \alpha}{3\epsilon_0} \qquad (2)$$

Where, ϵ_0 is the permittivity of free space, M_w is the molecular weight and, N_A is Avogadro's number and ρ is the density. In general, the dielectric constant, $\acute{\epsilon}$ increases by increasing the degree of polarizability, α, which depends on density, ρ,

cross-linking, free volume, and chemical coupling. Here, the paper discusses the effect of the dopant such as P, which, being a donor can get latched in between the conjugate chains of PI. Radiation-induced intra-chain coupling of phosphorus atoms thus effectively increases the dielectric constant, $\acute{\epsilon}$ of the PI.

It is further assumed that as a result of fluorine doping, the free volume of the PI must have increased because an appreciable number of the hydrogen atoms are replaced by fluorine atoms which are larger in size. It is known that the electric polarizability of a C—F bond is lower than that of the C—H bond [14]. The electronic polarization is assumed to have decreased with an increasing number of fluorine atoms in the PI. The plots in **Figure 4(b)** is reproduced from [58] indicates that the dielectric constant, $\acute{\epsilon}$, decreases with the increasing concentration of fluorine, but it is seen to increase with the increasing concentration of phosphorus in the PI. Boron is also assumed to increase the free volume in the chains of PI. As a result, the number of polarizable groups per unit volume has decreased with the increasing concentration of fluorine or boron atoms in PI.

4. Bulk and surface modifications by 6 MeV electron radiation

For 6 MeV irradiation, Mathakari et al. [64] used a PI sheet with a density ~ 1.43 gm/cm^3 and thickness of 50 μm. The sheet was cut into pieces of size 100 mm $\times$ 15 mm $\times$ 50 μm for stress-strain studies. Whereas for other characterizations, thin films of size 15 mm $\times$ 15 mm $\times$ 50 μm were used. The samples were irradiated with a 6 MeV electron beam obtained from the Race track microtron laboratory of the Department of Physics, University of Pune, India. The irradiation was performed in the air under normal thermodynamic conditions. The beam diameter was kept $\sim$15 mm and the strips were irradiated at the central location, for mechanical measurements. Whereas, for other samples of dimension 15 mm $\times$ 15 mm $\times$ 50 μm, they were exposed to the uniform electron beam. Electron fluence was varied in the range of 1–4$\times$ 10^{15} electrons/cm^2. Stopping power $\sim$ 1.836 MeV cm^2/g and range $\sim$2.36 cm for 6 MeV electrons in PI was calculated from the ESTAR program. Calculated doses from the stopping power and range were estimated to be 294–1176 kGy. Following this, pre and post-irradiated samples were characterized by various techniques. The irradiated strips used subjected to stress-strain measurements, carried out using a tensile testing machine (UTM). Testing parameters such as load cell, strain rate, and gauge length were, respectively, kept 100 kg, 20 mm/min, and 50 mm. For each pristine and irradiated, an average of measurements on four samples was taken. From obtained stress-strain profiles, numerous mechanical parameters like tensile strength, percentage elongation, strain energy, and Young's modulus were calculated. By measuring coordinates of breaking points on stress-strain profiles, the tensile strength, and percentage elongation were calculated, whereas, strain energy was calculated from the measured stress-strain curve area. Young's modulus was computed from the initial slope of stress-strain curve.

4.1 Mechanical analysis

Figure 6 displays recorded stress-strain profiles for PI irradiated with 6 MeV electrons. The stress-strain curve was distinctly becoming large with an increase in electron fluence and indicative of enhancement in mechanical properties of PI by electron irradiation.

Calculated mechanical parameters like tensile strength, % elongation, strain energy, and Youngs' modulus (from stress-strain profiles) are, respectively, shown in **Figure 7(a–d)**. Notably, tensile strength, percentage elongation, and strain energy is
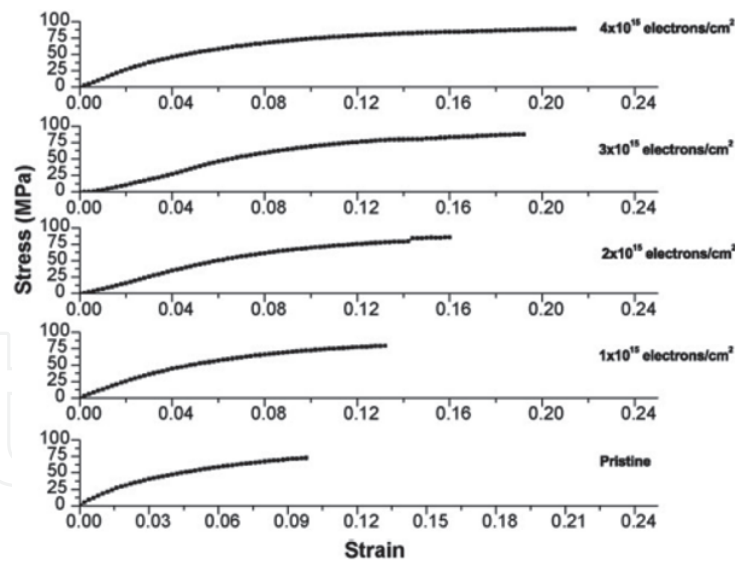
Figure 6.
Stress-strain profiles for pristine and 6 MeV electron irradiated PI. Reproduced with permission [Mathakari et al. [64] ©Copy right 2010, Materials Science and Engineering–B].
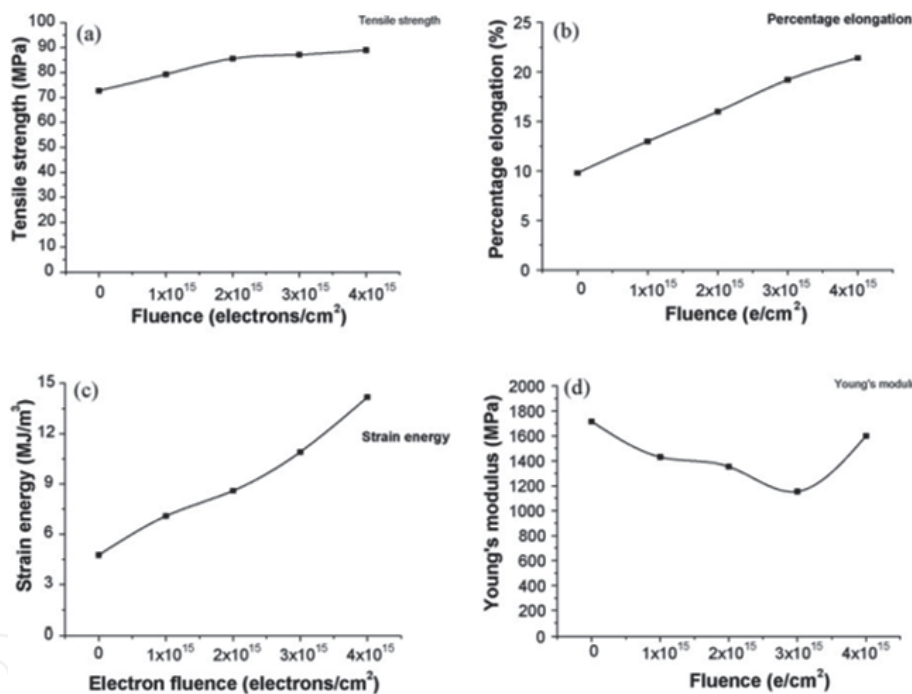
Figure 7.
Recorded profiles of (a) tensile strength, (b) percentage elongation, (c) strain energy, and (d) Young's modulus as a function of fluence for irradiated PI. Reproduced with permission Mathakari et al. [64] ©Copy right 2010, Materials Science and Engineering–B.

observed to be increased from the pristine values of 73–89 MPa, 10–22%, and 4.75–14.2 MJ/m^3, respectively, @ maximum value of fluence (4 × 10^{15} electrons/cm^2) with, corresponding, relative % increments noted to be 22%, 120%, and 199%. Enhancement in mechanical properties is attributed, fundamentally, to change in cross-linking. Upon irradiation, both scission and cross-linking take place in polymer simultaneously, and depending upon polymer, radiation type, and amount of dose rate scission and cross-linking, one or the other may dominate. From the obtained results, Mathakari et al. [64] were of the opinion that in their case cross-linking had dominated over scissioning. The dose rate of 6 MeV electrons was additionally high ~2000 kGy/h. In such a case scenario radiation density induced large area spurs (zones enriched with highly reactive free radicals) overlapping each other. This

results in free radicals cross-linking. Further, depending upon dose rate and extent of radiation-induced oxidation; the dominance of scission or cross-linking takes place. But the oxidative changes are weak when dose rates are high [21]. The presence of a large concentration of carbonyl groups in the PI monomer may offer high resistance to oxidation [65]. Thus, the high dose rate and carbonyl-assisted oxidation resistance of PI resulted in extremely low oxidative changes. And hence, crosslinking has dominated over scissioning. Notably, Mathakari et al. [64] observed enhancement in tensile strength, % elongation, strain energy, whereas, Youngs' modulus was found to be decreased, marginally, from the pristine value of 1700–1160 MPa @ 3×10^{15} electrons/cm^2 and then increased up to 1600 MPa @ 4×10^{15} electrons/cm^2. The overall decrease was reported to be 6% and attributed to an increase in % percentage elongation which was considerably larger than the increase in the value of tensile strength. This lead to a conclusion that 6 MeV electron irradiation has considerably enhanced chain dynamics in PI.

4.2 FTIR and UV-vis spectroscopy

Figure 8(a) displayed FTIR spectra recorded for pristine and electron irradiated PI@ different fluences. Peak @ 3085 cm^{-1} is assigned to C H stretching, carbonyl (CO, stretching) in PMDA is located between 172 and 1781 cm^{-1}, hydroxyl (OH) @ 3630 cm^{-1} whereas 1260–1289 cm^{-1} showed C—O—C str. in monomer ODA. Peaks @ 3486 and 1602 cm^{-1} are assigned to N—H str. and bend, respectively. The cyclic imide (C—N—CO) group was scrutinized using peaks that appeared @ 1376–1390 (C—N stretch). The imide stretching was observed @ 1380 and 1117 cm^{-1} and corresponding deformation @ 725 cm^{-1} [66, 67]. Mathakari et al. noted that the absorbance of almost all the bonds remains intact upto ∼4×10^{15} electrons/cm^2. That revealed scission and crosslinked products have the same absorption spectra as that of pristine PI. More importantly, absorbance at 1725–1781 cm^{-1} corresponding to carbonyl groups remained unchanged till maximum fluence which is indicative of the fact that PI is not oxidized after irradiation.

Further to reconfirm the absence of oxidation effects; **Figure 8(b)** shows only marginal variations in oxygen contents.

Figure 9 shows UV-vis spectra for pristine and electron irradiated PI. They noted, no marked changes in absorption edge and overall absorbance between 700 and 200 nm regions. By and large, PI showed a gradual red shift in the absorbance edge and overall increase in the absorbance due to carbonization and oxidation that confirmed bond structure retention of PI that has not undergone oxidation after irradiation.
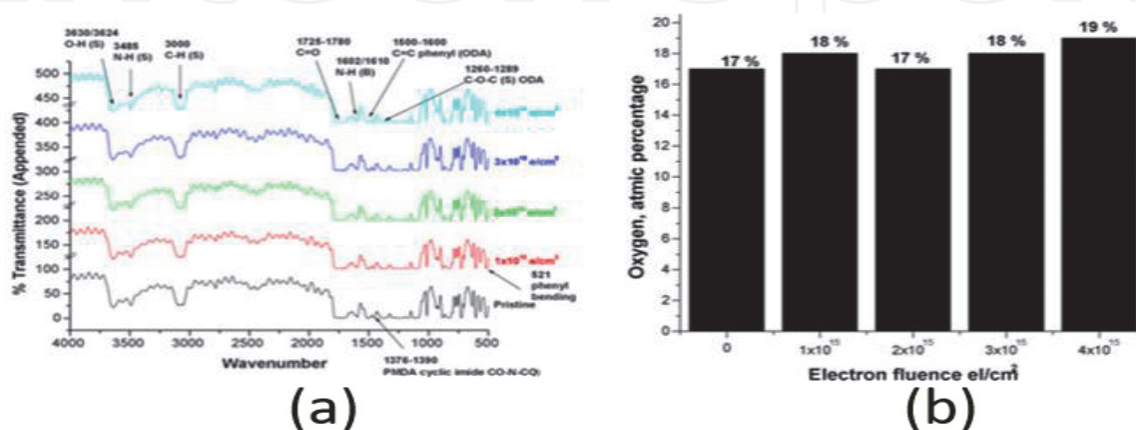
Figure 8.
Recorded (a) FTIR spectra and (b) for pristine and 6 MeV electron irradiated PI. Reproduced with permission Mathakari et al. [64] ©Copy right 2010, Materials Science and Engineering–B.
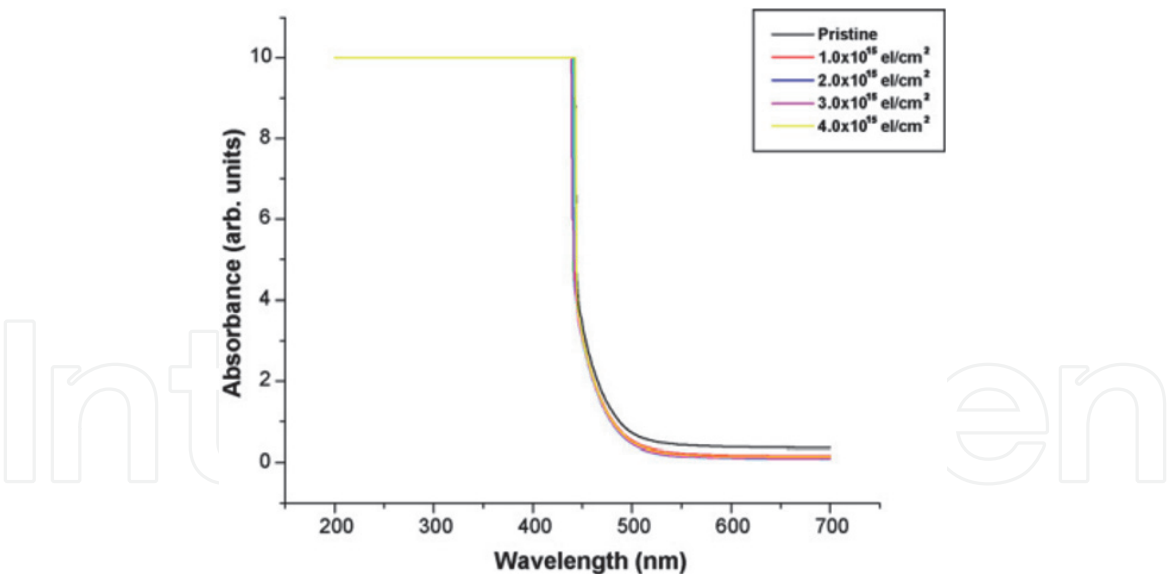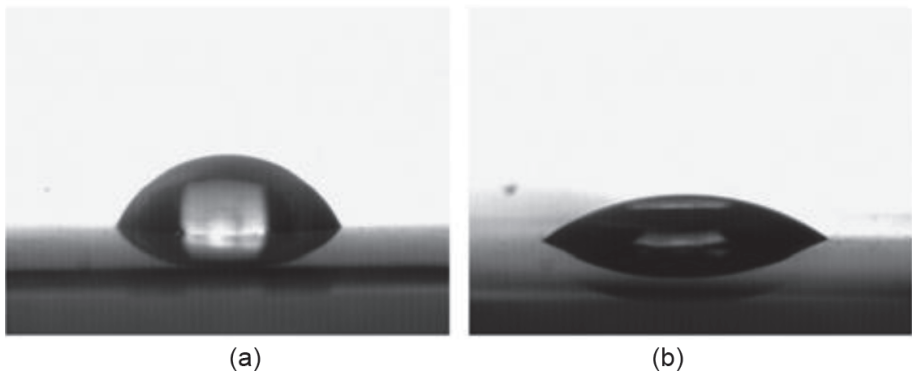
Figure 9.
Recorded UV-vis spectra for pristine and 6 MeV electron irradiated PI @ various fluences. Reproduced with permission Mathakari et al. [64] ©Copy right 2010, Materials Science and Engineering–B.

4.3 Contact angle studies

In **Figure 10**, reported by Mathakari et al., photographic images of distilling water droplet of volume ∼10 μl onto the surface of pristine and electron irradiated PI (@4×10^{15} electrons/cm^2 is shown. Data of contact angles, roughness, adhesion work, and area fraction of liquid-solid interface @ pristine and electron irradiated PI is provided in **Table 2**. They noted that contact angle decreased from its original (pristine) value of 59–32° @4×10^{15} electrons/cm^2. The observed reduction is ∼46% and indicative of significant surface modifications in PI surface by 6 MeV electrons. The work of adhesion, roughness and area fraction of the liquid-solid interface is found to be increased with the fluence.

From data of contact angle measurements, a significant reduction in contact angle is observed and, correspondingly, increase in work of adhesion and fractional area @ liquid-solid interface has, mainly, attributed to the radiation-induced surface roughening. By Wenzel formulation: cos Θ′ = r cos Θ, for hydrophilic surfaces contact angle decreases with an increase in surface roughness. The observed increase in roughness reveals that there is a greater amount of fractional are available for the contact @ solid/liquid interface [68, 69]. Both the enhanced parameters reduced the contact angle. Further, irradiation of PI surface may also cause the

(a)   (b)

Figure 10.
Photographic images of contact angle measurements displaying distilled water droplet of 10 μl volume onto the surfaces of (a) pristine and (b) 6 MeV electron irradiated PI@ 4×10^{15} electrons/cm^2. Reproduced with permission Mathakari et al. [28] ©Copy right 2010, Nuclear Instruments and Methods–B.

Polyimides

| Sr. no.	Fluence ($\times 10^{15}$)	Contact angle (°)	Roughness (r) cos $\Theta' = r \cos \Theta$	Adhesion work ($W_A = \gamma_{Lg}(1 + \cos \Theta)$)	Area fraction (f) @ liquid-solid interface $\cos \Theta' = f \cos \Theta + f - 1$
1	0.0	59	1.00	110.3	1.000
2	1.0	51	1.22	118.6	1.075
3	2.0	49	1.27	120.6	1.093
4	3.0	35	1.59	132.4	1.201
5	4.0	32	1.65	134.5	1.210

γ_{Lg} = surface tension of liquid-gas interface = 72.8 mJ/m². Θ = contact angle of the flat pristine sample. Θ' = contact angle of the rough sample after irradiation.
Reproduced with permission Mathakari et al. [28] ©Copy right 2010, Nuclear Instruments and Methods–B.

Table 2.
Data of contact angles, work of adhesion, and area fraction @ liquid-solid interface of pristine and 6 MeV electron irradiated PI.

opening of imide rings that lead to carboxylic acid and carboxamide formation. They might have played a significant role in reducing contact angle. Thus, a decrease in contact angle is indicative of the hydrophilic nature of PI surface facilitated by irradiation. Such peculiar surface properties with increased hydrophilicity can be used for a number of applications such as grafting, adsorption, or adhesion of organic or inorganic species onto the surface.

4.4 AFM and profilometry investigations

Thus, analysis of Mathakari et al., showed electron irradiation-induced surface roughening is responsible to reduce contact angle. This is reconfirmed in AFM and profilometry. **Figure 11** (upper pan) displays AFM images and (lower part) surface profilograms of pristine and electron irradiated PI@ 4×10^{15} electrons/cm². They
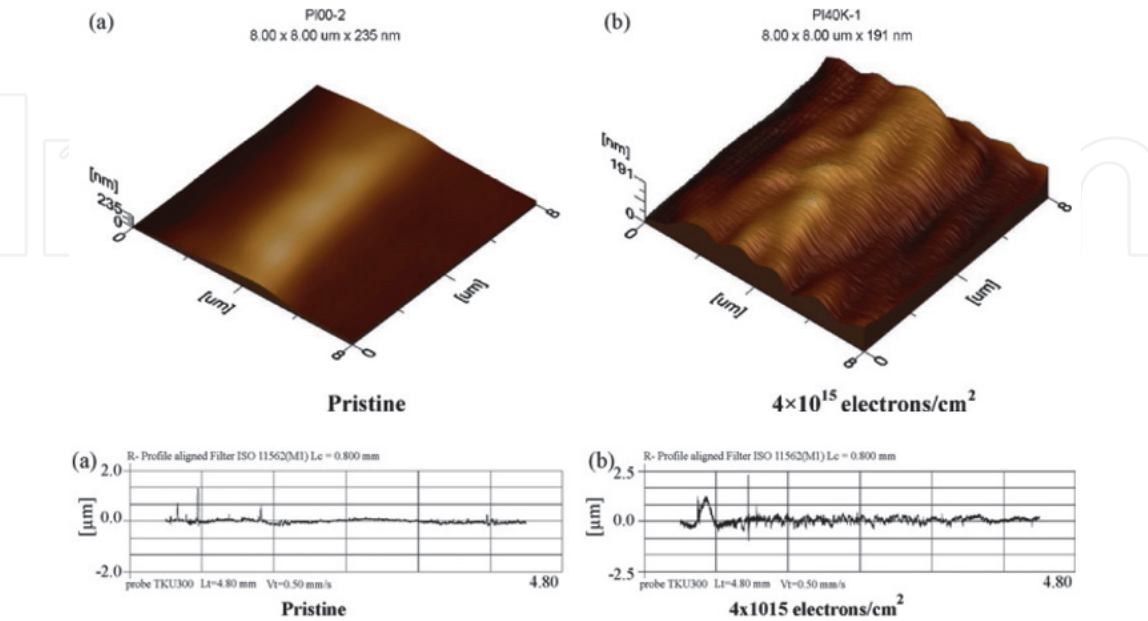
Figure 11.
Upperpart: AFM images (a) pristine and (b) 6 MeV electron irradiated PI at the fluence of 4×10^{15} electron/cm². Lower portion surface profile grams of (a) pristine and (b) 6 MeV electron irradiated PI at the fluence of 4×10^{15} electrons/cm². Reproduced with permission Mathakari et al. [64] ©Copy right 2010, Materials Science and Engineering–B.

14

noted the surface roughness enhancement after electron irradiation. And the average magnitude of roughness (Ra) is calculated from the profilograms as shown in **Figure 11**. The roughness is found to increase from 0.06 to 0.1 μm and is attributed to the electron beam-induced evolution of gases from the PI surface. The evolution of gases takes place in different regions to a different extent. Chain dynamics seems to be prominent on the surface causing scission and crosslinking in PI modifying surface properties. At bulk, this has implications on change in free volume and induces void type defects, which diffuse up onto the surface enhancing roughness [70].

In the next section, irradiation effects of oxygen ions on PI are discussed and vis-a-vis compared with fluorinated ethylene propylene (FEP).

5. Plasma effects: atomic oxygen

5.1 ECR plasma system

In a study carried out by Riyadh et al., atomic oxygen plasma ions are produced in Electron Cyclotron Resonance (ECR) plasma system. The system is comprised of two stainless steel chambers, one for generating microwave power-induced gas plasma and the other for sample irradiation by plasma. The plasma chamber is configured at a height of ~150 mm and dia. ~125 mm and also function as a microwave cavity resonator in TE111 mode. A magnetron (power ~ 500 W, freq. 2.45 GHz) was coupled to a plasma chamber through waveguides. The magnetic field required for generating the ECR plasma was produced via pair of solenoid coils, mounted around the plasma chamber. The irradiation chamber at a height of ~300 mm and a diameter of ~200 mm has numerous ports that were used for mounting different systems such as reaction gas injector, mechanical support to the samples holder, feed through for electrical measurements, vacuum gauges, window view, etc. The coupling between irradiation and plasma chamber was done in such a fashion that the ions produced in ECR plasma could directly interact with the samples mounted onto the irradiation chamber. In order to measure the energy and flux of oxygen ions, a three-grid retarding field analyzer (RFA) was mounted on the chamber. In both chambers, a pressure of $\sim 10^{-6}$ mbar was maintained with an appropriate vacuum system. A schematic design and irradiation setup for the ECR plasma system is shown in **Figure 12**.
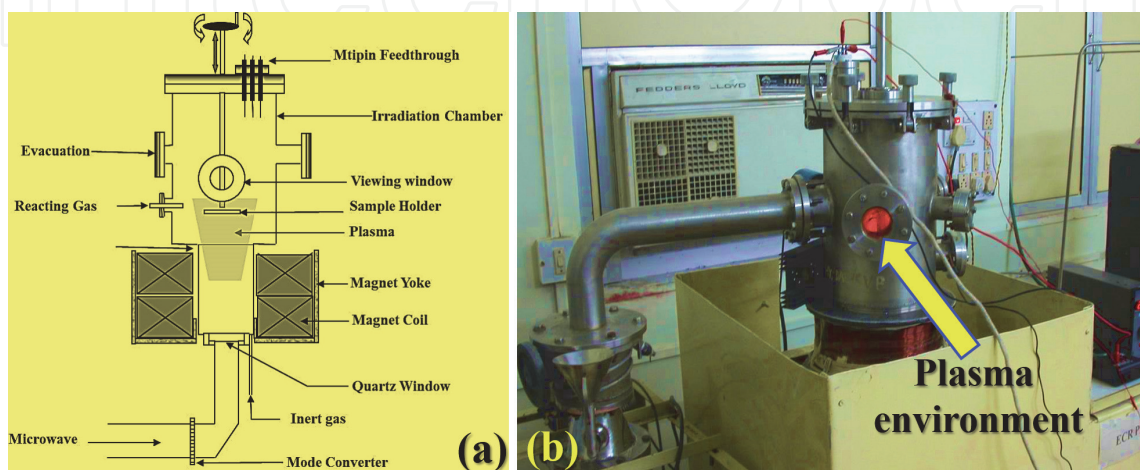
Figure 12.
(a) A schematic design, and (b) experimental set-up of ECR Plasma system. Reproduced with permission Riyadh et al. [55] ©Copy right 2006, Radiation Effects and Defects in Solids.

5.2 Sample preparation

For plasma treatment, PI and FEP samples were obtained by cutting ∼50 μm thick sheets into small pieces of dimension ∼15 × 15 mm². After cleaning and drying, the samples were stored in a dry and clean atmosphere. Before plasma treatment, the weight of each (PI and FEP) sample was measured by Riyadh et al. using a digital balance, with an accuracy of ±1 μg.

5.3 Irradiation with oxygen ions

After obtaining base pressure ∼10^{-6} mbar and making electrical connections, pure oxygen gas (99.9%) was inflected into the plasma chamber via a mass flow controller. Numerous experimental parameters like oxygen flow rate, microwave power, axial magnetic field, oxygen pressure, etc., were optimized to obtain a stable oxygen plasma into the reactor chamber. Energy and oxygen flux of plasma ions at certain positions along with the axial chamber position and @different pressures were measured using three grid RFA. Measurements were repeated and the system was calibrated for ion energy and flux at different positions of plasma. ECR plasma was also characterized by quadrupole mass spectrometry. The intensity of atomic oxygen ions was found to be almost one order of magnitude higher than that for molecular oxygen ions, at all the energies of oxygen ions. Since the abundance of atomic oxygen ions was very high compared to molecular oxygen ions. Four samples of PI and FEP were mounted on the sample holder such that the separation between two conjugate samples was ∼3 mm. Samples were, subsequently, irradiated with plasma at 8×10^{-3} mbar, at a position where the energy of plasma species was ∼10^{-14} eV. However, ion flux was maintained at maxima with an energy of ∼12 eV. The flux of ions with ∼12 eV of average energy was ∼5×10^{13} ions cm^{-2} s^{-1}. The sample holder was mounted onto insulating support that was functioned as a Faraday cage. A current integrator, connected to the sample holder, was used to measure a current due to ions received by samples during ion irradiation. Four samples at a time were exposed to oxygen ions at a flux of ∼5×10^{13} ions cm^{-2} s^{-1}. Ion fluence was varied by changing the time of irradiation that was estimated from the charge received by the samples during ion irradiation. Ion fluence was varied from sample to sample in a range ∼5×10^{16} to 2×10^{17} ions cm^{-2} with time. Plasma-treated samples were characterized by various techniques.

5.4 Weight-loss investigations

Riyadh et al. reported in **Figure 13** that, for both PI and FEP samples, weight loss was increased with increasing plasma exposure, t (s). They speculated a small amount of surface atoms got eroded out when plasma ions impinge onto the polymer surface. However, they noted that the cross-section of this process was small at the set ion energy. Another process noted was chemical reactions. In this atomic oxygen, ions interact with near-surface atoms and slash the weak bonds. This results in the evolution of gaseous species from polymers during plasma treatment. The observed weight loss in the polymer is therefore reported to be a combined effect of atoms that are removed from the surface and redeposited onto the surface during irradiation. The erosion yield (Ey) was calculated by equation [2]:

$$E_y = \frac{\Delta M}{(\rho A \Phi t)} \tag{3}$$
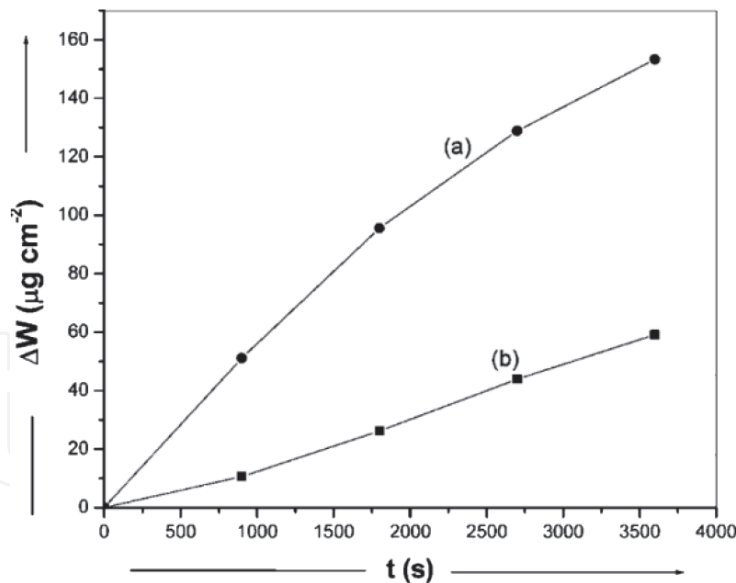
Figure 13.
Weight loss (ΔW) (µg/cm²) variations with time of exposure t (s) to the atomic oxygen ions at a flux of
$\sim5 \times 10^{13}$ *ions* $cm^{-2} s^{-1}$ *(a) PI (b) FEP. Reproduced with permission Riyadh et al. [55] ©Copy right 2006,*
Radiation Effects and Defects in Solids.

where, **Φ** is incident ion flux, M is mass loss (gm), ρ is matrix density (1.42 gm cm^{-3}(PI) and 2.15 gm cm^{-3}(FPE)), A is sample area (2.25 cm²), and t is the exposure time(s). In FEP weight loss is reported due to rupturing of CF_2 bonds and defluorination. After fluorine ejection, new bonds like C—O and C=O are possible to form in the surface region. Moreover, oxidation of C—F bonds is endothermic [33] for these processes. The erosion yield in FEP may be governed by various radiation-induced processes like breaking of chemical bonds and new bond formation, adsorption, or bonding of oxygen atoms to the polymer matrix. In this, the reaction efficiency of atomic oxygen with polymer surface depends upon the chemical composition and bond strength. The average erosion yield (Ey) for the PI is estimated to be $\sim7 \times 10^{-22}$ cm³ per atom and $\sim1.35 \times 10^{-22}$ cm³ per atom for FEP. Their results indicated that erosion yield for FEP is ~5 times lower than that for PI.

5.5 Morphological analysis: SEM

In **Figure 14** micrographs reported by Riyadh et al. shows image (1a) and (2a), revealing surface regions of virgin counterparts of PI and FEP. They were reported to be smooth and featureless. However, after plasma treatment, the surface texture
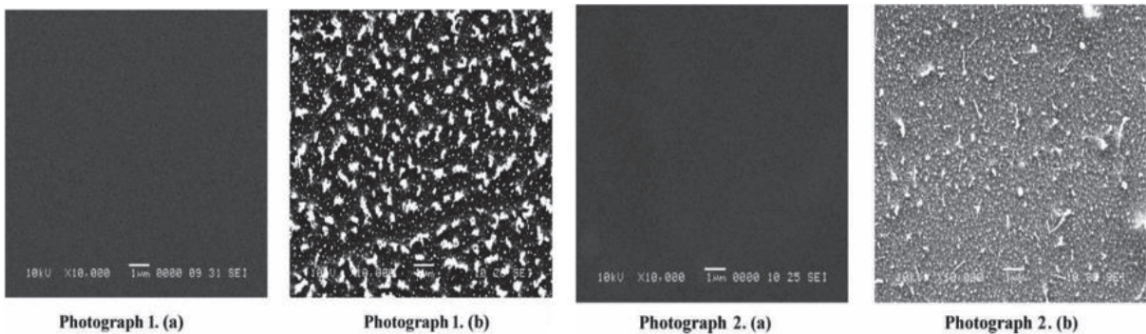
Figure 14.
Micrograph 1 is recorded SEM for (a) virgin PI, and (b) plasma-treated PI. Image 2: for (a) virgin FEP and (b) plasma-treated FPE. (@Ion fluence $\sim2 \times 10^{17}$ ions cm^{-2}). Reproduced with permission Riyadh et al. [55] ©Copy right 2006, Radiation Effects and Defects in Solids.

of PI exhibited blister formation and nano-particles of different dimensions. They confirmed that these changes are caused mainly due to variations in local erosion rates. On exposure to oxygen plasma, various gaseous moieties like hydrogen, nitrogen, oxygen, and fluorine could be evolved from the surface region of polymer. The blisters on the surface of PI were reported to be ~1.4 μm and nano-particles formed in FEP and PI were, respectively, of dimensions ~50 to ~80 nm. By and large, their results showed that on exposure to plasma degradation PI was greater than in FEP under identical irradiation conditions. The obtained results were found to be consistent with estimated values of erosion yield for FEP and the PI.

5.6 XPS investigations

Samples of PI and FEP were exposed to plasma ions for about 1 h, followed by characterization using the XPS technique. The data were deconvoluted using origin with Gaussian fittings and FWHM ~1.6 eV as trial value for deconvolution. Binding energies were calibrated with respect to C 1s peak @ 285 eV (binding energy) in order to compensate for surface charging effects. **Tables 3** and **4** summarize the results. Peaks for both, PI and FEP, were assigned as per literature reports [37, 38, 71–77]. Peaks corresponding to C=C, C—C, and C—H, bonds in aromatic rings of

	Binding energy (eV) atomic oxygen		
Sample	Virgin	Irradiated	Assignment
PI	288.5	288.7	Shake up
	286.4	286.8	C—O—C
	285.5	285.7	Aromatic ring
	284.6	284.9	Aromatic structure
	283.8	284.2	Benzene ring
FEP	285	284.7	C—C or C—H
	–	286.3	C—O
	–	288.6	C=O
	290.8	290.6	—CF
	292.9	292.5	—CF$_2$
	295	294.5	—CF$_3$

Reproduced with permission Riyadh et al. [55] ©Copy right 2006, Radiation Effects and Defects in Solids.

Table 3.
C-1s binding energy values estimated from XPS peaks for virgin and plasma-treated PI and FEP.

Sample		Concentration %								
		C 1s	O1s	N1s	F1s	C:O	C: N	O: N	F:C	O: F
PI	Virgin atomic oxygen irradiated	68.23	29.3	2.6	—	2.6:1	26.2:1	11.3:1	—	—
		80.9	17.5	1.6	—	4.6:1	50.6:1	10.9:1	—	—
FEP	Virgin atomic oxygen irradiated	32.6	2.1	—	65.3	10:06	—	—	2.1	0:0.03:1
		37.5	19.2	—	43.3				1:15:1	0.44:1

Reproduced with permission Riyadh et al. [55] ©Copy right 2006, Radiation Effects and Defects in Solids.

Table 4.
Concentration of elementals, their ratios for virgin and plasma-treated PI and FEP.

PI appeared at 283.8, 284.6, and 285.5 eV for virgin PI and at 284.2, 284.9, and 285.7 eV for plasma-treated PI, respectively. Peak position shift was indicative of modification in imide structure that revealed the opening of the backbone benzene ring. For aromatic carbon, peaks emerged at 286.4 eV (virgin PI) and at 286.8 eV (plasma-treated) were assigned for its bonding with oxygen. Peak intensity of 286.8 eV was reduced by ~50% compared to peak @ 286.4 eV. For virgin PI, peak at 288.5 and for plasma-treated PI peak @288.7 eV were assigned to a carbonyl group. They are also associated with esoteric and acidic functionality.

For virgin FEP, peaks at 285, 290.8, 292.9, and 295 eV were, respectively, assigned to C—H or C—C, —CF, —CF$_2$, and —CF$_3$ groups. Due to the large relative abundance of —CF$_2$; the presence of —CF and —CF$_3$was indistinguishable. For plasma-treated FEP, peaks @ 284.7, 286.3, 288.6, 290.6, 292.5, and 294.5 eV were, respectively, assigned to C—H or C—C, C—O, C=O, —CF, —CF$_2$, and —CF$_3$. For FEP, the intensity of —CF$_2$ peak was found to be reduced by ~60% compared to virgin counterpart. The formation of free radical species with oxygen; led to the emergence of prominent oxidized carbon signals. After plasma treatment, positions of carbon in PI were shifted to higher energy and in FEP to the lower side. This can be explained on the basis of bond weakening in polymers. **Table 3** shows for FEP two additional oxygen-related moieties were formed due to oxygen replacement by fluorine. By and large, oxygen is comparatively less electronegative than fluorine. Therefore, in FEP binding energies were shifted in the lower regime for C-1s, whereas, in PI, the binding energy shift at the higher side was due to weak electronegativity of hydrogen as compared to oxygen. The imide structure was found to be modified by plasma by breaking aromatic rings [77] and inducing polarization near carbon sites. These processes showed an increase in the binding energy of C-1s in the XPS peaks of the PI.

The ratios of C:O, C:N, and O:N for PI and ratios of F:C, C:O, and O:F for FEP are provided in **Table 4**. The values were obtained after normalizing the intensity of each XPS peak with respect to the corresponding photoelectric cross-section. They were indicative of an increase in the concentration of carbon, whereas, reduction in O and N for plasma-treated samples. For hydrogen, XPS is relatively insensitive, and atomic oxygen and hydrogen are reactive to form water vapors out diffusing from a carbonaceous layer of polymer.

In PI, an increase in the ratio of C:N from 26.2:1 up to 50.6:1 for post-treated samples was attributed to atomic oxygen interactions with C—N bonds [77] and the formation of new C—O—N species. However, it was speculated that during plasma exposure, C—O—N bonding would be broken leading to new species like NOx on PI surface that might have been pumped out of the reactor. Desorption of water vapors and NO$_x$ species leads to a reduction in N and O with enhancement in C by plasma exposure. For FEP surfaces plasma treatment showed a significant increase in O, with a marginal increase in C including an appreciable reduction in F. This resulted in an increase in ratios of O:C and O:F on surfaces of plasma-treated FEP.

5.7 Vibration spectroscopy analysis

Figure 15 showed that, peaks in FTIR spectra recorded for virgin and plasma-treated PI (a) C—O stretching @ 1050–1250 cm^{-1}, (b) C—C backbone aromatic ring @ 1504 cm^{-1}, (c) N—H bend @ 1602 cm^{-1}, (d) carbonyl stretch @ 1724 cm^{-1}, and (e) O—H and N—H stretch @ 3080–2872 cm^{-1} [77]. They were similar to each other, except for small changes in intensities. Spectrum provided bulk information that was not so prominent in the surface region. Overall reduction in peak intensities was attributed to changes in the surface region mainly due to the erosion factor. **Figure 15** showed that peaks appeared at (a) 680–780 cm^{-1} were due to the presence of weaker band bending for C—F group, (b) @ 980 cm^{-1} due to —C—C—
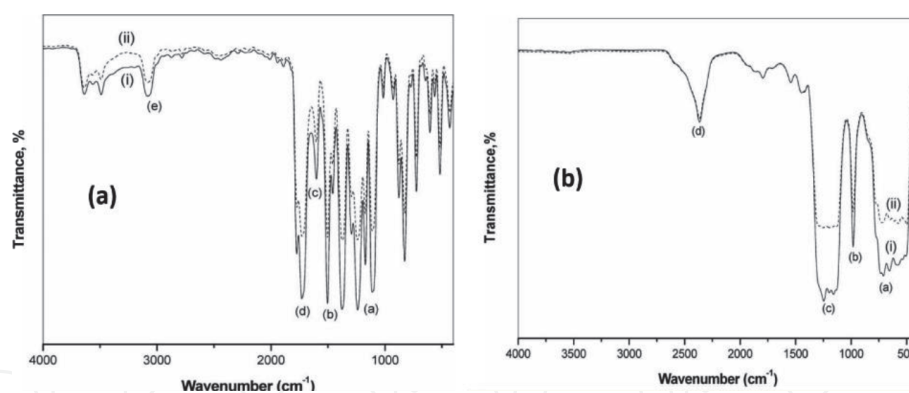
Figure 15.
FTIR recorded for (a) (i) virgin and (ii) plasma-treated PI, (b) (i) virgin and (ii) plasma-treated FEP (all @ 2 × 10¹⁷ ions cm⁻²). Reproduced with permission Riyadh et al. [55] ©Copy right 2006, Radiation Effects and Defects in Solids.

stretch in side-chain C—CF$_3$ group, (c) @ 1100–1400 cm^{-1} for C—F coupled to C—C stretch, and (d) @2370 cm^{-1} for —CF$_2$ stretch [78–80].

For plasma-treated FEP, peak intensities were lowered with slight modifications in shape when compared with virgin FEP. Their results of FTIR supported the results of weight loss, SEM, and XPS for PI and FEP. The decrease in peak intensities revealed that the corresponding concentration of moieties had lowered due to atomic erosion from the polymer surface. From FTIR spectra of virgin and plasma-treated PI showed in **Figure 15**, it is clearly observed that the intensities of the absorption peaks at 1050–1250, 1504, 1602, 1724, and 3080–2872 cm^{-1} corresponding to C—O, C—C, N—H, C=O, and O—H, respectively, have decreased after exposure to atomic oxygen ions. Similarly, from the FTIR spectra of FEP shown in **Figure 15**, it is observed that the intensities of the C—F peaks at 680–780, 980, and 1100–1400 cm^{-1} have decreased after exposure to atomic oxygen ions. It is clear from these FTIR spectra that the bonds are more or less equally affected in FEP and PI after exposure to the atomic oxygen ions. However, the absorption peaks corresponding to O—H and N—H bonds showed a significant loss in the peak intensity. Their results, therefore, indicated that weight loss in PI was higher than in FEP. XPS analysis also revealed that C—O peak intensities in PI and intensities corresponding to fluorocarbon bonds in FEP have decreased, significantly, after exposure to plasma. Overall FTIR revealed that surface and sub-surface regions of PI and FEP were modified due to atomic erosion. Notably, the surface of FEP was reported to be more resistant to plasma attack. Riyadh et al. speculated that diffusion of fluorine into surface layers of PI may provide protection against atomic oxygen radiation degradation and have promised in space applications.

6. Synergetic effects: electrons + atomic oxygen

In this work, carried out by Majeed et al., samples of dimensions 15 mm × 15 mm × 50 μm were cut out from a PI sheet. The irradiation with electron beam was carried out by keeping samples inside a thin-walled polyethylene bottle mounted on the Faraday cup cage. From Race-track-microtron of Pune University, India, a pulsed electron beam of energy 1-MeV energy was obtained with pulse width ~ 1.6 μs and pulse repetition rate 50 pps. Beam was scattered elastically by a thin tungsten foil of thickness ~40 μm in order to obtain a uniform intensity on samples. The intensity of beam uniformity over a circular area of ~40 mm was measured to be ~5%. A current integrator, mounted in the system was used to measure electron flux incident on Faraday cup. Four different electron fluences 0.5, 1.0, 1.5 and 2.0 × 10¹⁵ e/cm^2 were

chosen with constant flux. Thus, by varying irradiation time, electron-fluence was changed followed by exposure to plasma flux at different fluences of atomic oxygen ions. The experimentation was carried out in a separate setup. In this, reference samples were PI taken to be samples without electron irradiation.

For atomic oxygen plasma treatment, experiments were carried out in the in-house-developed, microwave-based Electron Cyclotron Resonance (ECR) plasma system as described in Section 5.1, **Figure 12**. The specific parameters such as energy and ion flux, in ECR plasma at different axial positions of the chamber. Chamber pressure variations were measured using a three-grid retarding field analyzer (RFA) as reported in our earlier publication [55]. For plasma treatment, samples were irradiated at an operating pressure of 8×10^{-3} mbar, at maximum energy position (10–14 eV) of oxygen ion with maximum flux ($\sim 5 \times 10^{13}$ ions cm^{-2} s^{-1}) with mean energy $\sim$12 eV. Plasma was also characterized by a quadrupole mass spectrometer. They noted almost one order magnitude of variation at the higher side in the intensity of atomic oxygen ions than that of molecular oxygen over the entire energy range. Thus, they reported an abundance of molecular oxygen-less compared to atomic oxygen. Total fluence was varied by time variations in sample exposure, covering a range 5–20×10^{16} ions cm^{-2}.

Gravimetric measurements of virgin and radiation treated (electron + plasma) were performed using a microbalance with an accuracy of ± 1 μg.

Surface-wetting characteristics with de-ionized water were estimated by measuring contact angle "θ" in which measurements were performed with NRL-C. A. goniometer (RameHart. Inc. USA) with an optical protractor. Wettability measurements were immediately performed after removing samples from the plasma chamber. The wettability technique used was the sessile drop technique with 2 μl droplet volume. Three measurements were taken and values reported by Majeed et al. were the mean value of three measurements recorded for each sample. Measurement accuracy was ± 1 degree. The work of adhesion (WA) related to surface wettability was calculated which is [81] is given by: $W_A = \gamma_{LV} (1 + \cos\theta)$, where, LV is interfacial surface tension @ liquid/vapor interface, and θ is contact angle (LV = 72.8 mJ/m^2 for water).

Figure 16 shows variations in weight loss in % with plasma exposure time. Net weight loss in virgin PI was reported to be increased with plasma exposure time.
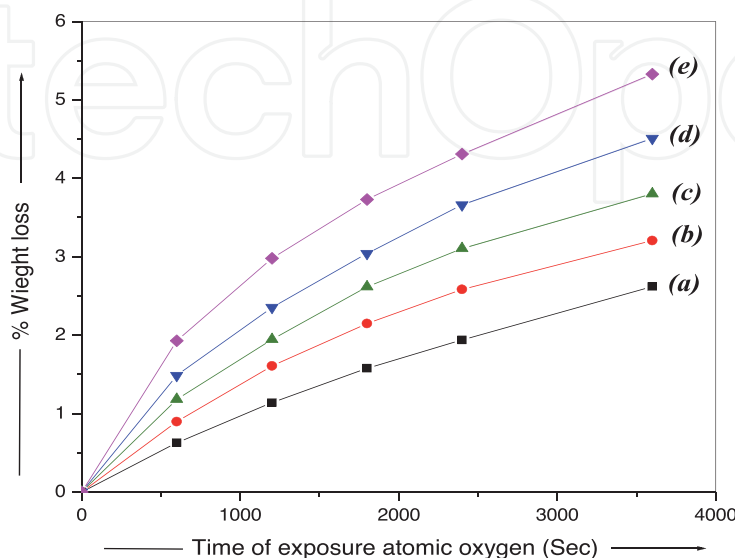
Figure 16.
Variations in % weight loss with plasma exposure for equivalent flux $\sim 5 \times 10^{13}$ ions cm^{-2} s^{-1}, for PI irradiated with 1 MeV electrons @ fluences: (a) 0 to (e) 20 $\times 10^{14}$ e/cm^2. Reproduced with permission Riyadh et al. [55] ©Copy right 2006, Radiation Effects and Defects in Solids.

Notably, for 1 MeV electron-irradiated PI rate of weight loss increased with increasing fluence of electron irradiation.

6.1 Investigations on atomic oxygen erosion

Erosion (volume per atom) yield quantification was carried out using the expression: $E_y = \Delta M / (\rho.A.\Phi.t)$, where, ΔM is mass variation, ρ, is density (1.42 gm cm^{-3}), A is sample area, ϕ is oxygen ion flux, and t is exposure time. The average erosion yield, Ey, was determined to be $\sim 7.05 \times 10^{-22}$ cm^3 $atom^{-1}$ for virgin PI and $\sim 14.26 \times 10^{-22}$ cm^3 $atom^{-1}$ for electron irradiated PI. **Table 5** displays values of Ey obtained for electron irradiated PI @ different fluence.

Data revealed that, average erosion yield after exposing PI to electrons has increased by a factor of 2 as compared to virgin PI which was indicative of PI upon electron irradiation becomes more susceptible to plasma erosion.

In order to reveal the nature of radiation-induced surface modifications; hydrophilic characteristics of polymer surface were investigated by measuring wettability. Wettability depends upon surface roughness and surface chemical composition. Change in surface properties was, in turn, reflected in modification in measured contact angle. **Figure 17** shows variations in contact angle plasma exposure time, for PI irradiated with 1 MeV electrons @different fluences. They noted a reduction in

Fluence of 1 MeV electron ($\times 10^{14}$ e/cm^2)	Maximum erosion yield ($\times 10^{-22}$ cm^3 atom^{-1}) (accuracy 1%)
0 (virgin)	7.28
5	8.92
10	10.56
15	12.53
20	14.81

Table 5.
Maximum erosion yield (E_y) for PI irradiated @ different electron fluences with subsequent exposure to oxygen plasma flux@ $\sim 5 \times 10^{13}$ ions cm^{-2} s^{-1}. Reproduced with permission Riyadh et al. [55] ©Copy right 2006, Radiation Effects and Defects in Solids.
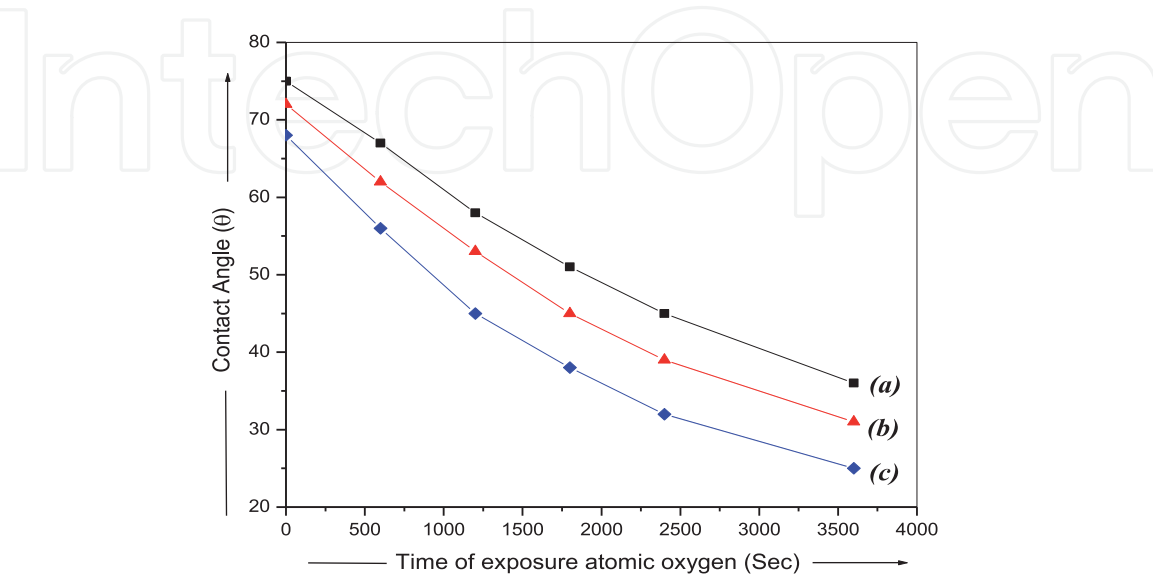
Figure 17.
Contact angle variations with plasma exposure (@ $\sim 5 \times 10^{13}$ ions cm^{-2} s^{-1} flux) for PI irradiated with 1 MeV electrons with fluences: (a) 0 (virgin), (b) 10 $\times 10^{14}$ e/cm^2, and (c) 20 $\times 10^{14}$ e/cm^2. Reproduced with permission Riyadh et al. [55] ©Copy right 2006, Radiation Effects and Defects in Solids.

| Time of exposure (s) | Virgin PI samples | | 1 MeV electrons irradiated samples at fluence | | | |
| | | | (10 × 10¹⁴ e/cm²) | | (20 × 10¹⁴ e/cm²) | |
	Contact angle"θ" (°)	Work of adhesion (W$_A$) mJ/m²	Contact angle"θ" (°)	Work of adhesion (W$_A$) mJ/m²	Contact angle"θ" (°)	Work of adhesion (W$_A$) mJ/m²
0	75	91.6 ± 1.3	72	95.3 ± 1.2	68	100.1 ± 1.2
600	67	101.2 ± 1.2	62	107 ± 1.1	56	113.5 ± 1.1
1200	58	111.4 ± 1.1	53	116.6 ± 1.0	45	124.3 ± 0.9
1800	51	118.6 ± 1.0	45	124.3 ± 0.9	38	130.2 ± 0.8
2400	45	124.3 ± 0.9	39	129.4 ± 0.8	32	134.5 ± 0.7
3600	36	131.7 ± 0.7	31	135.2 ± 0.7	25	138.8 ± 0.5

Reproduced with permission Riyadh et al. [55] ©Copy right 2006, Radiation Effects and Defects in Solids.

Table 6.
Data for θ and W$_A$ for virgin and electron irradiated PI before and after plasma exposure for different periods of time.

water contact angle, θ, to a larger extent as compared to virgin PI. Corresponding W$_A$ was calculated and displayed in **Table 6**.

The obtained data was indicative of θ change with W$_A$ for electron irradiated PI which was observed to be much higher than that for virgin reference. Significant reduction in θ with improved wettability was mainly attributed to electron irradiation-induced surface modifications.

Morphological analysis was carried out by investigating changes in surface roughness. In **Figure 18(a)** and **(b)**, SEM micrographs, comparatively show surface-morphologies of PI exposed to plasma; with and without electron
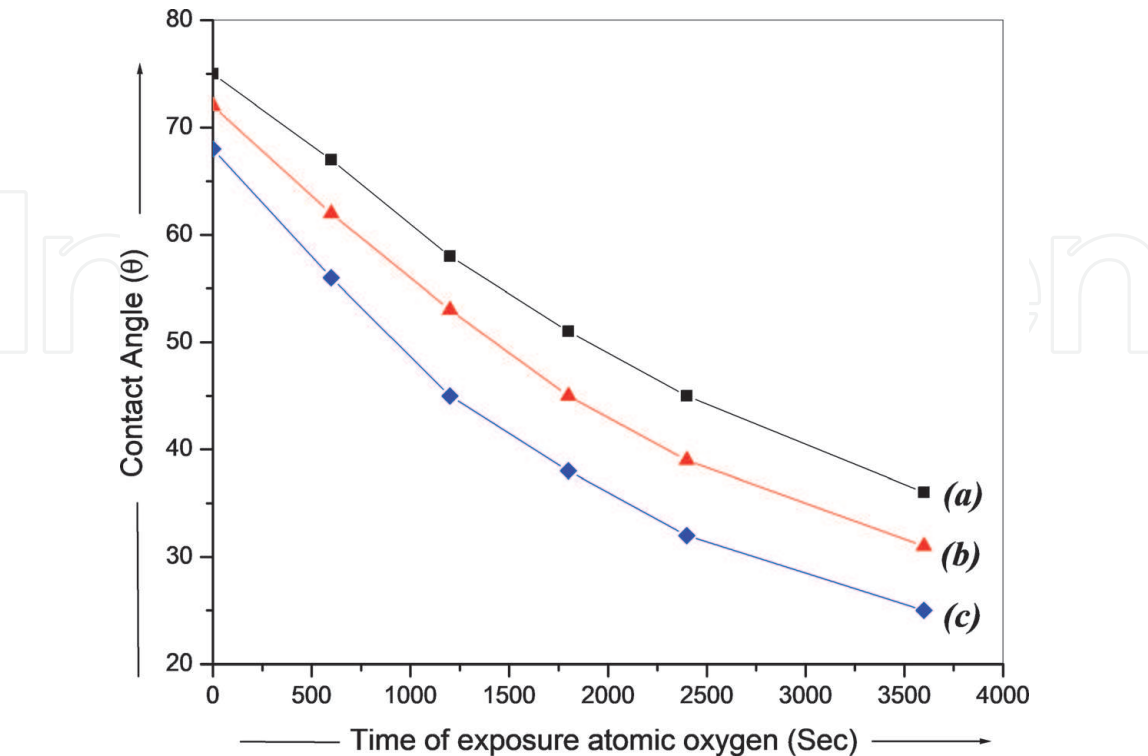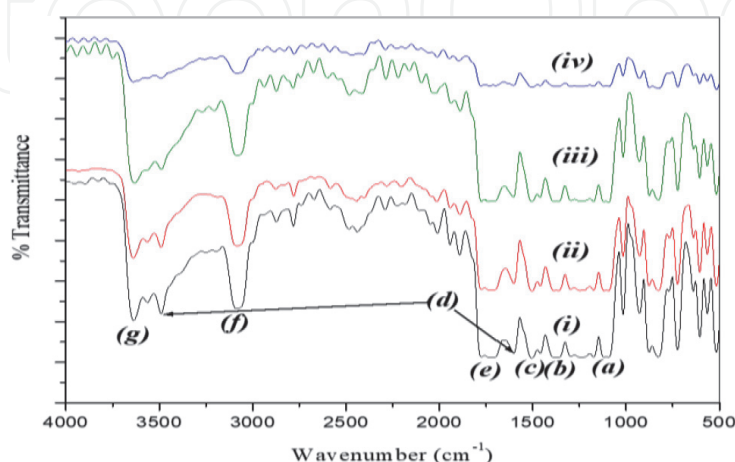

Figure 18.
SEM micrographs: (a-i) virgin, (a-ii) plasma treated (@ 2 × 10¹⁷ ions cm⁻²), (b-i) electron irradiated, (b-ii) combined (electron + plasma treated) @ 2 × 10¹⁷ ions cm⁻². Electron fluence @ 20 × 10¹⁴ e/cm²for both samples in (b). Reproduced with permission [52] Copy right 2006, Radiation Effects and Defects in Solids.

pre-irradiation. Although surface roughness was noted to be enhanced marginally when pre-irradiated alone (b-i) or oxygen alone (a-ii). However, for electron irradiated surfaces (@ 20×10^{14} e/cm^2) that were subjected to plasma (@ 2×10^{17} ions cm^{-2}) a drastic change in surface roughness was observed, as seen in (b-ii). The surface texture of electron-irradiated PI that was subsequently exposed to plasma was observed to consist of globules, cavities, and blisters of various sizes. This may be attributed to synergetic electron-irradiation and plasma-induced surface erosion in PI. Majeed et al. reported that defects introduced in the surface region by electron irradiation indent roughness which became more susceptible to oxidative erosion by plasma treatment. The chain scission process seems to be responsible for causing surface degassing from the samples. Due to the coagulation of emerging molecular species, blisters were formed. Nonuniform degassing may lead to significant surface roughness. They reported secondary effects too such as chain scission might have re-crosslinked leading to a subsequent change in surface free volume, which resulted in the imperfect surface after radiation [52] treatment.

As discussed earlier, polymer on encountering energetic radiations breaks in chain and link as well simultaneously. However, chain scission or cross-linking depends upon the type of polymer, radiation, and dose rate. As reported in earlier literature [52] it appears that MeV electrons can effectively produce cross-linking in PI. Moreover, the dose rate of electrons is considerably high. In such cases radiation density induced zones nucleates in reactive free radicals that expand and get overlapped resulting in cross-linking of free radicals. Moreover, the dominance of scission or cross-linking also depends upon the extent of radiation-induced oxidation.

The combined effect of radiation-induced changes was further analyzed by Majeed et al., using vibrational i.e. FTIR spectroscopy. **Figure 19** shows recorded FTIR spectra for and electron-irradiated PI before and after exposure plasma exposure. Four spectra are displayed in the figure. Basic spectrum corresponds to virgin i.e. profile (i), (ii) plasma-treated, (iii) electron irradiated, (iv) combined electrons + oxygen plasma. Intensities in (i), can be compared with those in other spectra. Prominent absorption was observed corresponding to (a) C—O str. @ 1050–1250 cm^{-1} (b) CO—N—CO cyclic imide appeared @1376–1390 (=C—N str.), (c) C—C backbone aromatic ring @ 1504 cm^{-1}, (d) N—H bend. and str., respectively, @1602 cm^{-1} and 3486 cm^{-1}, (e) carbonyl str. @ 1724–1780 cm^{-1}, (f) C—H str. @ 3085 cm^{-1}, and (g) hydroxyl —O—H @ 3630 cm^{-1} [66, 82, 83]. By and large, Majeed et al., noted a marginal reduction in intensities of almost all emerged bands

Figure 19.
Recorded FTIR spectra of PI for (i) virgin, (ii) plasma treated @ 2×10^{17} ions cm^{-2}, (iii) pre-electron-irradiated @ 20×10^{14} e/cm^2, and (iv) electrons (@ 20×10^{14} e/cm^2 + plasma (@ 2×10^{17} ions cm^{-2}) treated. (a) to (g) indicate assigned functional groups described in the text. Reproduced with permission Riyadh et al. [55] ©Copy right 2006, Radiation Effects and Defects in Solids.
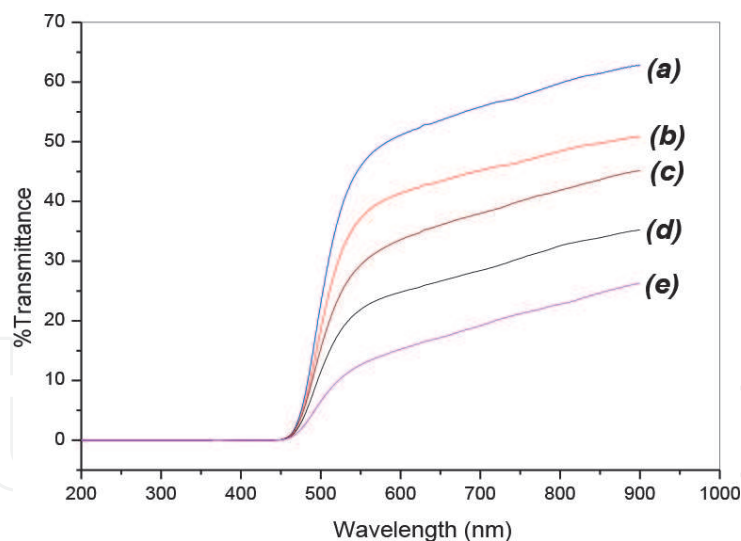
Figure 20.
UV-visible transmission spectra of (a) virgin, (b) plasma treated, (c) electron irradiated + plasma treated (plasma @ 1 × 10¹⁷ ions cm⁻²) (d) plasma treated, (e) electrons + plasma treated (plasma @ 2 × 10¹⁷ ions cm⁻²). Reproduced with permission Riyadh et al. [55] ©Copy right 2006, Radiation Effects and Defects in Solids.

on exposure of the thin film to plasma, whereas, electron alone affected to a lesser extent showing shallow changes in absorption peaks. In contrast, IR absorption bands were extensively reduced for combined electrons and plasma effects. This showed electron irradiation alone does not extensively contribute to chain scission or cross-linking, whereas, plasma irradiation is capable of producing chain scission as well as cross-linking by the reactive oxidation process. This process got further prominent if the ionizing electron irradiation has created defect centers. As reported earlier, atomic oxygen reacts with C—N species which is the weakest bond in PI, and establishes C—O—N bonding.

Figure 20 showed UV visible transmission spectra of PI @ different radiation conditions. A combination of two doses (electron + plasma) was presented. The plots showed that the value of % transmission was observed to be decreased when PI got treated with electrons + plasma combinedly as compared to plasma alone. Thus, synergetic effects were operational by electrons irradiation causing surface erosion, and apparently plasma treatment effectively enhanced the roughness of polymer films. Such a rough surface was responsible to enhance light scattering and thus reducing the overall transmission property of the sample.

7. Ion track technology: production parameters

7.1 Techniques of track etching

In a study carried out by Alegaonkar et al., common polymer foils were used such as polyethylene terephthalate (PET), PI (PI), polycarbonate (PC), and silicone rubber, however, due to space crunch, herein, we have presented only the results of 10–20 μm thick PET and PI films (Goodfellows Ltd., Russian). These films were irradiated with 300–500 MeV Ar, Kr, Xe ions over the fluence 1–500 × 10⁶ cm⁻²@ heavy ion accelerator @JINR Dubna (Russia) or @ HMI Berlin (Germany).

By and large, the choice of the projectile and its energy provides magnitude and distribution of transferred energy density along the ion track trail, which consequently determines the track-to-bulk etching rate. It also influences the shape of emerging pores called etched ion tracks (post-etching). For PET irradiated under

certain conditions and etched in a typical condition yields rather cylindrical tracks, whereas, for PI conical (or hyperbolical if etched from both sides) had been reported. The angle of cone, χ, was observed to be increased with reducing an atomic number of projectile ion, $\chi \sim 20°$ for PI. Post latent track etching of PET films was carried out using 3 mole/l NaOH at 45°C. Systematic observations on the etching track shapes were made in a regular time interval using ion transmission spectrometry (ITS) [84]. ITS technique records the energy spectrum of nearly monoenergetic (5.49 MeV) α particles from a 40 kBq^{241}Am α source, transmitted through the etched films. With sequential etching, when for the first time α particles get transmitted through the etching film without any energy loss it is indicative of etching breakthrough can be achieved. One can calculate track radius, provided that one knows the areal track density [85]. The tracks etching has been done up to diameters in a range of $\sim$100 nm and a few µm.

7.2 Production of metallic tracks: chemical deposition

By deposition of Ag, Cu, and Ni, we have carried out the production of conducting etched ion tracks. We adopted the chemical or electrodeless deposition (ELD) technique in order to deposit metal within the etched tracks [86]. Particularly for Cu and Ni deposition, we used commercially available solutions from M/s Doduco Ltd. Whereas, for deposition of Ag, we followed the reported procedure of St. Gobain (Brockhaus, 1895; Th Pone, 1955), due to the green approach. Deposition of Cu and Ag was carried out at 24°C, and Ni @ $\sim$88°C. Martin et al. [86] reported a strong surface-near reduction of the inner track diameter including the closure of track, however, we have not observed any such thing.

7.3 Nucleation centers

7.3.1 Chemical activation

In order to achieve durable metal layers on polymeric substrates, it requires the existence of nucleation centers on polymer surfaces where the metal atoms could be deposited. For polymers used herein, for metal precipitation and nucleation the areal density intrinsic surface defects were too low for the formation of a continuous metallic layer. This led to the emergence of discontinuous metal tracks as seen
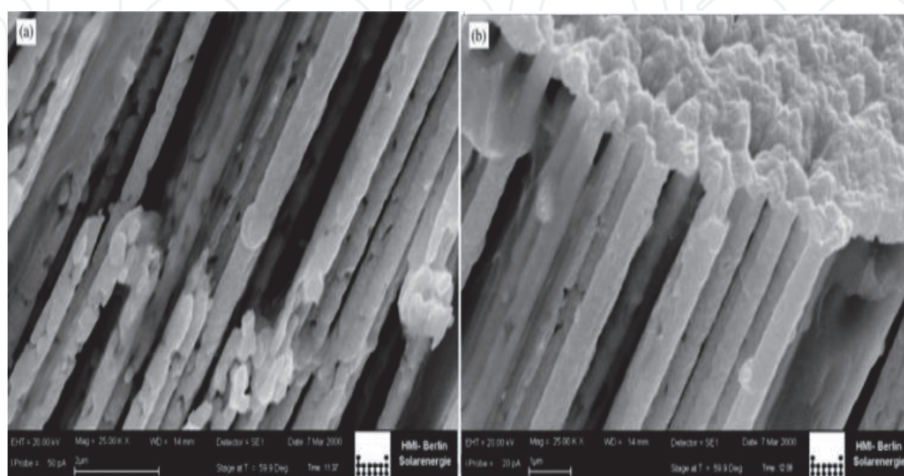
Figure 21.
Comparison of SEM micrographs for (a) intermittent and (b) continuous ELD-deposited tracks of Ag in PET. In this, image (a) shows preparation of deposition without activation, and image (b) displays the addition of chemical activation centers. Reproduced with permission Fink et al. [6] ©Copy right 2004, Radiation Effects and Defects in Solids.

in **Figure 21(a)**. The creation of additional nucleation centers was observed to be generating continuous track tubules as seen in **Figure 21(b)**. One can achieve this by surface activation process either chemically by bonding suitable metal atoms (e.g. Sn, Pd) or physically by creating dangling surface states by laser or ion irradiation.

We have carried out resistivity measurements along the track axis to assess the quality of emerging track deposition. This was carried out by contacting the front and rear sides of the etched track polymer films using Au electrodes under constant gentle pressure. Initially, high-track resistivities were registered. In order to determine very low track resistivities, some polymer films were irradiated through mask pinholes to reduce the areal density of tracks (which were counted).

Figure 22 shows the dependence of Cu-filled track quality with activation time that revealed a necessity to introduce a sufficient number of nucleation centers. For non-activated samples, the resistivity was (not shown here) closely resembled samples of 1s activation time (**Figure 22**). Analysis exclusively revealed that the metal was deposited onto intrinsic defects. From **Figure 22**, it can be seen that after the exposure for a few seconds the process of activation improves the track quality by orders of magnitude. On saturation of density of nucleation centers, exposure of polymer film to the activation solution is ineffective. Thus, the quality of metallic track-tubules is correlated to the roughness of their inner surfaces. During the initial track, tubule growth surface area is larger and nucleation centers were less available. For smooth inner tubule walls with high conductivity, a high nucleation center density is a basic requirement. Moreover, the roughness of inner walls of the etched track, depending on the etching conditions such as etchant concentration; the smoothness of the outer tubule surfaces can be determined) and is of utmost importance. This is demonstrated by comparing the quality of metal-filled tubules in PET and PI prepared under identical conditions. We noted the filled track tubules in PI were better due to the greater smoothness of both inner and outer tubule walls.

7.3.2 Formation of nucleation centers by ion irradiation

In addition to chemical activation, another channel is ion irradiation. The underlying mechanism is to activate ring structures in polymer by electronic energy transfer so that oxygen can be attached. This will facilitate metal addition. The nucleation center formation experimentation for 30–300 keV He+ to Xe+ ions was performed that resulted in polymer surface activation @fluences of 10^{13} cm^{-2} and
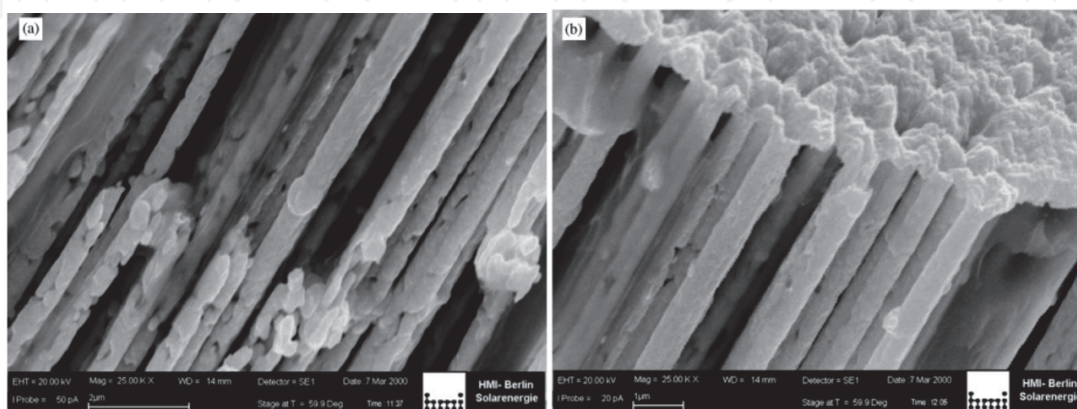
Figure 22.
Variation in resistivity of tracks in PE and PI films with embedded Cu material along the surface normal to the film (i.e. along the axis of ion track). Conditions for chemical activation and ELD deposition: 5 min ELD solution exposure. Reproduced with permission [6] Copyright 2006, Radiation Effects and Defects in Solids.

was noted to be independent of projectile ion. No saturation in surface activation was observed due to irradiation.

Morphological investigation revealed that metal layers deposited onto ion-activated polymers were appeared to be smoother compared to the chemically activated nucleation process. They concluded ion-induced activation took place locally which enabled to tailoring of the metal deposition along the axis of the track. It means for a cylindrical metal contact embedded in tracks can be produced on both sides of a track for sensor application.

7.3.3 Characterizations of tubule

For metals, ELD deposition took place in track tubules after a system-dependent specific incubation time (Ni ∼ 5 s, Ag ∼ 1 min, Cu ∼ 11.2 min). However, at higher temperatures, the track deposition and tubule formation speed were observed to be fast [8]. **Figure 23** via-a-vis compares the rate of deposition of ELD at room temperature within the etched ion tracks with unirradiated polymer surfaces. However, within the tubule, metal layers started growing ∼2 times earlier than that on pristine surfaces which were attributed to the higher activation density of etched tracks. The irradiation-induced damage at the inner walls of the track were bonded the sensitizers better than inert pristine surfaces. For both tubules and pristine surfaces deposition showed a steadily decreasing deposition trend with an increase in time. This was attributed to exhaust of available solutions and the complete filling up of narrow tracks. No significant difference was observed for pristine surfaces and tubule walls of any radius, which that demonstrated, the diffusion speed of ELD solution within very narrow tracks has not a decisive parameter. A dramatic change in their electric conductivity was noted for increased metallization of filled tracked films. During the initial stage of deposition, the fall in resistivity was seen by orders
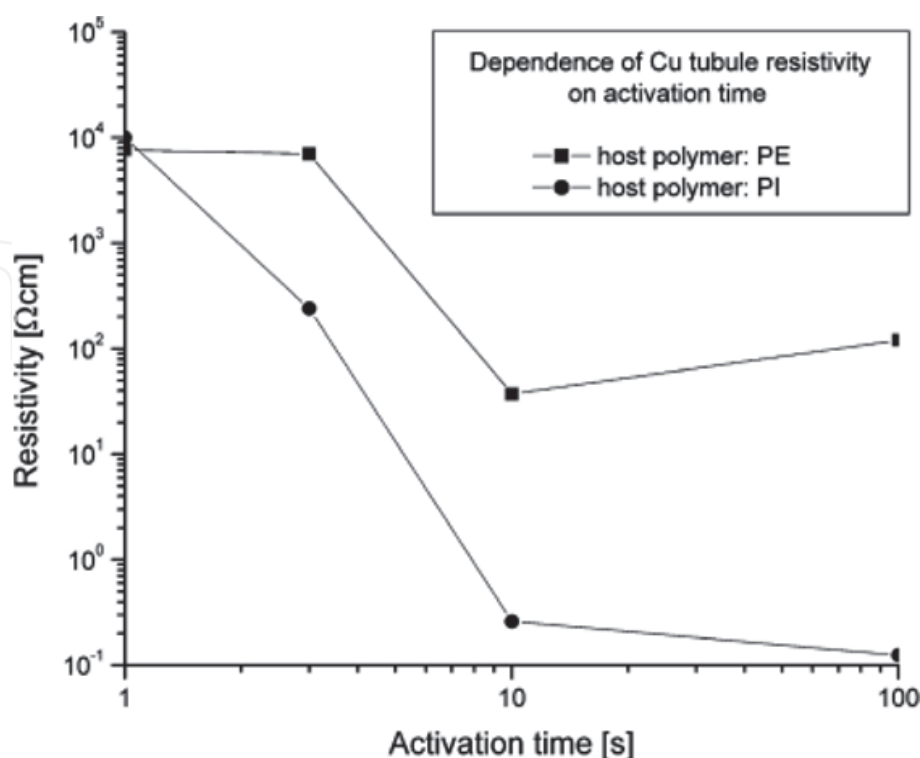
Figure 23.
Metallic layers deposition and growth in PI track by ELD. Comparison for deposition in pristine polymer films and growth at the interior of etched tracks, for Cu and Ni deposition. Reproduced with permission [6] Copyright 2006, Radiation Effects and Defects in Solids.

of magnitude from dielectric to semiconducting to conducting regime with the gradual development of continuous metal layer. Thus, further reduction in resistivity was determined by the increase in layer thickness. Inside the tracks, the resistivity was observed to be improved faster than on the surface of the thin film. This observation was consistent with the rise in the growth of metal layers within the tracks.

By and large, we were able to prove by SEM, conductivity studies, and ITS measurements that metallic tubules tracks were continuous and hollow throughout the track height of the polymer film. However, measurements of Rutherford backscattering revealed marginal variation in thickness of tubule wall along the axis of track.

7.4 Thermal stability of etched tracks and metallic nanotubules

There is number of proposals for ion track applications that required high-temperature stability either during device preparation or actual implementation, for such purpose behavior of the tracks and their embedded structures must be known. As a first examination of this kind is already reported in reference [87]. According to reported findings, etched tracks of PE initially gots welled a bit upon heating due to release of moisture (received from the etchant) and subsequently became thin due to onset flow of glassy polymer, and towards the end got widen again swiftly due to carbonization. As a result, silver-filled track tubules appeared to be lost in their parallel alignment above the glass transition temperature (T_g) so that their transmission rapidly decreased upon annealing. However, for PI, developed ion tracks were observed to be maintained their shapes up to ~450°C, and thereafter, transformed with the onset of carbonization. They were observed to be increased in their width. Silver-filled PI tracks were observed to be led to a stable structure >600°C.

8. Applications of ion tracks

Above discussion clarifies the role and application of latent (as-implanted ion tracks) and etched tracks. Broadly speaking, latent tracks are emerged fundamentally due to the deposition of high energy (MeV to GeV) inside a tiny volume element called as the core of the ion track which has volume 10^{-15}–10^{-14} cm^3. Moreover, within an impulsive time, about 10^{-17}–10^{-15} s interaction by swift heavy ions, these exceptional transient conditions, led to a dramatic variation within materials. These changes are chemical and structural in origin that accompanies heat and pressure impulse. Primary damage such as transient breaking of all bonds is recovered during generated annealing phase followed immediately after the ion impact, named, thermal spike in about 10^{-12}–10^{-11} s. However, a number of irreversible changes remained within the damaged cylindrical zone. Thus, such zone is altered with characteristic changes like accumulation of high density of radicals, excess carbonaceous clusters, new phases (SiC in polysilane), amorphization, and modification in inherent free volume. As a result, several macroscopic properties of the irradiated polymer could get modified like permeability, refraction index, electric conductivity, thermal properties, etc.

For such damaged zone i.e. latent tracks, there are four major strategies showed up: (1) exploiting modified transport properties along the tracks, (2) precipitation of metallic atoms or clusters along the damaged zone, (3) exploiting chemical changes in polymer, and (4) using phase transition characteristics induced by ion irradiation [88]. Hitherto insignificant work has been carried out in these fields. In

general, ion-irradiated polymer films carrying latent tracks can be used as a seal in order to protect sensitive zones against penetration of ambient dust and moisture; maintaining equilibrium pressure and exchange of gases with ambiance. There are very few reports presenting proof of concept like doping of latent tracks for electronic application [85], SiC needles [88, 89] for AFM cantilevers, ion-induced conducting nanowires in diamond [90], or fullerite [88] for field emission displays are demonstrated.

8.1 Manipulations with etched tracks: flat flexible devices

Dissolving latent track material by suitable agents, termed as an etching process, led to the formation of the etched track. For this, there is a combo pack of projectile selection, targeted polymer, etchant, and etching conditions. Further, etched tracks can be manipulated in the desired shape like cylindrical, conical, hyperbolic, transmittent, non-transmittent. In principle, etched ion track can be filled by a number of material, and embedded assembly of material can be assembled as bulky wires, termed as, fibers or fibrils or tubules. In this, metal could be dispersed discontinuously in the form of nanoparticles along with the track geometry. The initial step could be realized by embedding matter within etched tracks to transport material clusters towards the required position which could be accomplished by dissolving material of interest in a suitable aqueous or non-aqueous solution followed by penetration of the solution into the etched tracks by capillarity action. By allowing liquid to evaporate within the tracks, followed by dissolution of matter could result in a supersaturated state of metal particles which led to precipitate onto form tubule. There was number of reported tubules like KCl, C_{60}, polymethyl methacrylate (PMMA), dyes, etc. The thickness of the tubule depends, empirically, depends upon the amount of matter dissolved in a solvent and transported into the ion track.

The class of such deposition is called as chemical or electrodeless (ELD) deposition technique [91]. In this, high degree of supersaturation of certain metals like Cu, Ag, Au, Ni, etc., or metal chalcogenide like CdS, PbS, Cu_xS, ZnS, CdSe, ZnSe, CdTe, CuInSe2, etc., could be achieved by dissolving them in a suitable agent such as NH_3, ethylenediamine (EN), nitrilotriacetate (NTA), thiourea (TU), and others. They precipitate heterogeneously to generate tubules of these materials in etched ion tracks which possess nucleation centers activated chemically or physically or chemically as discussed earlier.

Further, colloidal possess specific optical and electronic properties like high charge storage capacity, fluorescence, polarization, etc., blending colloidal with etched track could lead to new interesting applications like colloidal of TiO_2, and $LiNbO_3$ (20 nm: ball milled) to form nanotubules in etched tracks for optical sensors. Moreover, solver colloidal of conducting silver paste was used to deposit etched tracks that yielded conducting micro/nanowires for etched ion-track with diameter five times larger than silver particles. In etched ion tracks, it is possible to deposit material by carrying out chemical reactions like the formation of photosensitive AgBr, by allowing chemical reaction between $AgNO_3$ and NaBr within etched ion tracks in which tracks were acted as microreactors. However, the hydrophilic nature of tracks puts requirements on penetrants to have wetting characteristics. For hydrophobic solvents such as liquid metals, one can use a pressure injection route to enter solvent forcedly into the nanopores. Eventually, this could be useful in modifying the wettability characteristics of etched track walls by suitable deposits. We observed that liquid Pb/Sn solder material could readily be penetrated into etched ion tracks, therefore, can be used for contacting ion-track-based devices for Cu-filled tracks.

Further, galvanic deposition is another deposition technique that was reportedly used to coat conducting matter within etched tracks. In general, etched microporous polymeric films could be connected to the cathode such that the deposited metal or conducting polymer grows throughout etched tracks generating non-porous rods. However, a major disadvantage in all track manipulation techniques using solvents was noted to be the formation of ionic radical e.g. Ag tubules in PI possess a weak halo of Na^+ (etchant) and Ag^+ (ELD) ions contributing weak ionic bulk conductivity. Etched ion tracks can also be deposited by gas-phase pyrolysis type reactions, permeating gas to transform solid residues such as carbon or silicon, via pyrolytic reactions. However, such reactions required high reaction temperatures, and etched tracks in PI, mica, and SiO_2 were found to be well-suited candidates. Evaporation also led to a limited deposition near the entrance of the ion track and having a demerit of limited depth that can be reached in narrow tracks by evaporation [92]. Semiconducting material filling in ultra-small dimensional tracks, exhibited diode characteristics with quantum effects such as resonant electron tunneling in which current/ voltage characteristics exhibited characteristic local maxima and minima over the applied voltage range. Capacitive coupling of such semiconducting ion track wires led to the formation of field-effect transistor-like structures. Especially, surface-modified metal ion track nanotubules were reported to be used to control electrolytic permissivity [93]. Moreover, such nanotubules grafted with gels were performed like switches for penetrating liquids [94]. Au nanotubules were used as miniaturized electrolytic sensors for detecting oxygen concentration. They were also used for in vivo long-time drug storage [95]. TiO_2 nanotubules were found to be advantageous in Li batteries [96] and fullerene tubules were reported to be effective
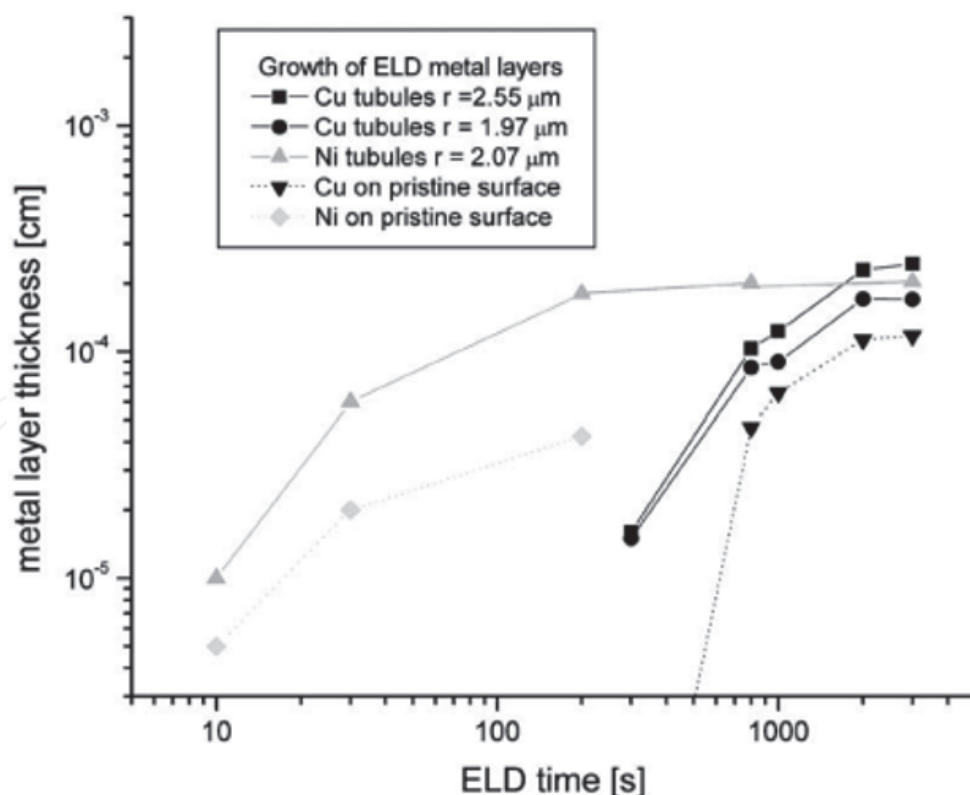
Figure 24.
Etched ion-track-based magnets and transformers, Left panel (a) prototype magnet with dimensions
$6 \times 7 \times 0:02$ mm³, deposition masks (above) and production steps (below); (b) comparison of input (bottom)
and output (top) signals of the transformer prototype, for rectangular and sinusoidal input at different
frequencies. The reasonable functional form is recorded in MHz frequency range (upper graph), but the signal
transformation is possible up to the near-GHz range when gradually a phase lag emerges between input and
output signals; (c) first miniaturized ion-track-based transformer of $1:2 \times 0:25 \times 0:01$ mm³ size. Reproduced
with permission Fink et al. [8] ©Copy right 2006, Radiation Effects and Defects in Solids.

temperature, pressure, and humidity sensors [97]. Layer-by-layer galvanic deposition of distinct materials led to axially structured elements such as Cu and Se [98, 99], or Ni and CdSe/CdTe [100] showed nano-diode characteristics, whereas, sequential galvanic deposition of different ferromagnetic materials led to giant magnetic resonance, GMR [101]. Layer-by-layer chemical deposition of semiconductor/metal/semiconductor led to the formation of cylindrical diodes, and metal/insulator/metal structures resulted in concentric condensers [102].

Architecting copper metal wires into etched ion tracks with sequential evaporation of metal contact stripes onto the surface of microporous polymer film led to the formation of micro-inductors (**Figure 24a**) and micro-transformers. Correspondingly, masks used for evaporation and intermediate production stages of a prototype magnet are displayed in **Figure 24a**. Corresponding test transformers show good operation up to ~0.5 GHz (**Figure 24b**), with inductances per winding of 10^{-4} H @ 10 Hz and 2.5×10^{-7} H @10^4 and 5×10^8 Hz with Q-factor approaching up to ~10. The miniaturized ion-track-based transformer is shown in **Figure 24c**. In a similar fashion combining lithography and etched tracks, miniaturized magnetic field sensors based on magneto-resistive ion tracks were produced by another research group [101]. First, ion-track-based sensors were developed especially for oxygen, as some biochemically important materials to be detected reacts with the enzyme glucose oxidase towards H_2O_2 which was transformed to water by anodic oxidation. Also, temperature, pressure, and humidity sensors were developed with C_{60} as a sensor material [97, 103].

9. Conclusions

In conclusion; the modification in various electrical and physicochemical properties of polyimide is shown to be induced by novel methods; without changing the major chemistry of the polymer. Most of the reported investigations are related to the irradiation effects of 50 μm thick, space quality film of polyimide by high energy electrons, gamma rays from Co-60, swift heavy ions, and low energy ions of atomic oxygen generated from the plasma source. Extracts of experimental details and the results have been presented in brief and are comprised in five separate sections (Sections 2–7) of the chapter.

The effects of electron irradiation on the dielectric properties were compared with those obtained from diffusing certain elements such as fluorine, boron, and phosphorous by radiation assisted diffusion process. The dielectric constant and the refractive index are shown to be lowered by irradiating the samples with 1 MeV electrons. It was seen to be further lowered when PI was doped with boron and fluorine even into a thin (3 μm) surface layer on both sides of the film. However, similar diffusion of phosphorous has been reported to increase the dielectric constant from 3.15 to 4.5. In these studies, the RBS technique was used for depth profiling wherein XPS for finding the chemical changes occurring in the surface layers. The variations in the dielectric constant and dielectric loss obtained with Co-60 gamma rays were similar to those obtained with 1 MeV electrons at a fluence of 10^{15} e/cm^2. These results are important in view of using 50 μm thick PI in space applications since the space vehicle is exposed to different kinds of radiations where lower values of dielectric constant are preferred. It is noteworthy that the diffusion of phosphorus or boron and fluorine was carried out at room temperature and the phenomenon of the tailoring of the dielectric characteristics of PI was found to be surface sensitive.

There are reports wherein the mechanical properties of PI were found sensitive to the radiations. Noticeable enhancement in the tensile strength was observed

when PI was irradiated with 1MeV electrons and this effect is attributed to the radiation-induced cross-linking. In addition, the electron beam-induced surface roughening was found to enhance the hydrophilicity of PI surface. In conclusion, it is proved that high-energy electron irradiation can be used to tailor the bulk and surface properties of PI.

Being a space-compatible polymer, PI has a special role to play in supersonic aircraft and in space vehicles. However, there is always a concern about its possible degradation on exposure to the atomic oxygen species during its passage in LEO. The paper discusses the various effects of AO, generated in a home-built Electron Cyclotron Resonance plasma system, on the surface erosion properties. It is noticed that degree of the surface degradation in FEP is lower, by a factor of five than in PI. The synergetic effects of 1 MeV electron irradiation and exposure to AO irradiation of PI have been discussed in detail. Electron irradiation has been found to be more detrimental to the surface erosion behavior by AO. The surface defects arising from chain-scission and cross-linking in PI by electrons are set responsible for the increase in the erosion yield.

Our earlier studies related to the production and behavior of metal nanostructures by chemically filling the etched ion tracks (produced by swift high energy ions) in PI have been elaborated. The results have proved the strength of the method for future devices. These reports indicate that the Etched Ion Tracks, in combination with lithography, opens up the possibilities for creating novel micro-structures in PI which is inaccessible by other techniques.

Acknowledgements

Author details

Prashant S. Alegaonkar[1*], Vasant N. Bhoraskar[2] and Sudha V. Bhoraskar[2]

1 Department of Physics, School of Basics Sciences, Central University of Punjab, Bathinda, Punjab, India

2 Department of Physics, Savitribai Phule Pune University, Pune, Maharashtra, India

*Address all correspondence to: prashant.alegaonkar@gmail.com

IntechOpen

References

[1] Iredale R, Ward C, Hamerton I. Modern advances in bismaleimide resin technology: A 21st century perspective on the chemistry of addition polyimides. Progress in Polymer Science. 2017;**69**: 1-21. DOI: 10.1016/j.progpolymsci. 2016.12.002

[2] Murphy C. Polyimides: Synthesis, Applications and Research. New York: Nova Science Publishers; 2016

[3] Ghosh MK, Mittal KL. Polyimides: Fundamentals and Applications. New York: Marcel Dekker; 1996

[4] Tribble AC. The Space Environment: Implementation for Spacecraft Design. Princeton, NJ: Priceton University Press; 1995

[5] Grossman E, Gouzman I. Space environment effects on polymers in low earth orbit. Nuclear Instruments and Methods in Physics Research Section B. 2003;**208**:48. DOI: 10.1016/S0168-583X (03)00640-2

[6] Fink D, Petrov A, Rao V, Wilhelm M, Demyanov S, Szimkowiak P, et al. Production parameters for the formation of metallic nanotubules in etched tracks. Radiation Measurements. 2003;**36**(1-6):751-755. DOI: 10.1016/ S1350-4487(03)00209-9

[7] Martin C. Nanomaterials: A membrane-based synthetic approach. Science. 1994;**266**(5193):1961-1966. DOI: 10.1126/science.266.5193.1961

[8] Fink D, Alegaonkar PS, Petrov AV, Berdinsky AS, Rao V, Müller M, et al. The emergence of new ion tract applications. Radiation Measurements. 2003;**36**(1-6):605-609

[9] Xu G, Gryte C, Nowick A, Li S, Pak Y, Greenbaum SG. Dielectric relaxation and deuteron NMR of water in polyimide films. Journal of Applied Physics. 1989;**66**(11):5290-5296. DOI: 10.1063/1.343719

[10] McCrum NG, Read BE, Williams G. Anelastic and Dielectric Effects in Polymeric Solids. Vol. 126. New York: Wiley; 1967

[11] Cha H, Hedrick J, DiPietro R, Blume T, Beyers R, Yoon DY. Structures and dielectric properties of thin polyimide films with nano-foam morphology. Applied Physics Letters. 1996;**68**(14): 1930-1932. DOI: 10.1063/1.115629

[12] Maruo Y, Sasaki S, Tamamura T. Change in refractive index and in chemical state of electron beam irradiated fluorinated polyimide films. Journal of Vacuum Science & Technology A: Vacuum, Surfaces, and Films. 1995;**13**(6): 2758-2763. DOI: 10.1116/1.579701

[13] Todd M, Shi F. Characterizing the interphase dielectric constant of polymer composite materials: Effect of chemical coupling agents. Journal of Applied Physics. 2003;**94**(7):4551-4557. DOI: 10.1063/1.1604961

[14] Hougham G, Tesoro G, Shaw J. Synthesis and properties of highly fluorinated polyimides. Macromolecules. 1994;**27**(13): 3642-3649. DOI: 10.1021/ma00091a028

[15] Hougham G, Tesoro G, Viehbeck A. Influence of free volume change on the relative permittivity and refractive index in fluoropolyimides. Macromolecules. 1996;**29**(10):3453-3456

[16] Hougham G, Tesoro G, Viehbeck A, Chapple-Sokol J. Polarization effects of fluorine on the relative permittivity in polyimides. Macromolecules. 1994; **27**(21):5964-5971

[17] Shih D, Yeh H, Paraszczak J, Lewis J, Graham W, Nunes S, et al. Factors affecting the interconnection resistance

and yield in multilayer polyimide/ copper structures. IEEE Transactions on Components, Hybrids, and Manufacturing Technology. 1993;**16**(1): 74-88. DOI: 10.1109/33.214864

[18] Laghari J, Hammoud A. A brief survey of radiation effects on polymer dielectrics. IEEE Transactions on Nuclear Science. 1990;**37**(2):1076-1083. DOI: 10.1109/TNS.1990.574201

[19] Clough R. Nuclear instruments and methods in physics research section B: Beam interactions with materials and atoms. 2001;**185**(1-4):8-33

[20] Chmielewski A, Haji-Saeid M. Radiation technologies: Past, present and future. Radiation Physics and Chemistry. 2004;**71**(1-2):17-21. DOI: 10.1016/j.radphyschem. 2004.05.040

[21] Cleland M, Parks L, Cheng S. Nuclear Instruments and Methods in Physics Research Section B. Applications for radiation processing of materials. 2003;**208**:66-73

[22] Fintzou A, Badeka A, Kontominas M, Riganakos K. Changes in physicochemical and mechanical properties of γ-irradiated polypropylene syringes as a function of irradiation dose. Radiation Physics and Chemistry. 2006;**75**(1):87-97. DOI: 10.1016/j. radphyschem.2005.03.014

[23] Švorčík V, Rybka V, Hnatowicz V, Novotna M, Vognar M. Electron beam modification of polyethylene and polystyrene. Journal of Applied Polymer Science. 1997;**64**(13): 2529-2533. DOI: 10.1002/(SICI) 1097-4628(19970627)64:13< 2529::AID-APP6>3.0.CO;2-F

[24] Hill D, Hopewell J. Effects of 3 MeV proton irradiation on the mechanical properties of polyimide films. Radiation Physics and Chemistry. 1996;**48**(5): 533-537. DOI: 10.1016/0969-806X(96) 00073-4

[25] Mishra R, Tripathy S, Dwivedi K, Khathing D, Ghosh S, Müller M. Fink: Spectroscopic and thermal studies of electron irradiated polyimide. Radiation Measurements. 2003;**36**(1-6):621-624. DOI: 10.1016/S1350-4487(03)00212-9

[26] Sasuga T, Hayakawa N, Yoshida K, Hagiwara M. Degradation in tensile properties of aromatic polymers by electron beam irradiation. Polymer. 1985;**26**(7):1039-1045. DOI: 10.1016/ 0032-3861(85)90226-5

[27] Kucheyev S, Felter T, Anthamatten M, Bradby J. Deformation behavior of ion-irradiated polyimide. Applied Physics Letters. 2004;**85**(5): 733-735. DOI: 10.1063/1.1776618

[28] Mathakari N, Bhoraskar V, Dhole S. MeV energy electron beam induced damage in isotactic polypropylene. Nuclear Instruments and Methods in Physics Research B. 2008;**266**:3075-3080. DOI: 10.1016/j.nimb.2008.03.165

[29] Lappan U, Geißler U, Häußler L, Jehnichen D, Pompe G, Lunkwitz K. Radiation-induced branching and crosslinking of poly (tetrafluoroethylene) (PTFE). Nuclear Instruments and Methods in Physics Research Section B: Beam Interactions with Materials and Atoms. 2001;**185**(1-4):178-183. DOI: 10.1016/S0168-583X(01)00751-0

[30] Millinchuk AV. Sixth international symposium on materials in a space environment. The Netherlands: ESTEC, Noordwijk; 1994. p. 253

[31] Wolan J, Hoflund G. Chemical and structural alterations induced at Kapton® surfaces by air exposures following atomic oxygen or 1 keV Ar+ treatments. Journal of Vacuum Science & Technology A: Vacuum, Surfaces, and Films. 1999;**17**(2):662-664. DOI: 10.1116/1.582027

[32] Milinchuk V, Klinshpont E, Shelukhov I, Smirnova T, Pasevich O.

Degradation of polymer materials in low earth orbits. High Energy Chemistry. 2004;**38**(1):8-12. DOI: 10.1023/B: HIEC.0000012057.54231.9b

[33] Packirisamy S, Schwam D, Litt M. Atomic oxygen resistant coatings for low earth orbit space structures. Journal of Materials Science. 1995;**30**(2): 308-320. DOI: 10.1007/BF00354390

[34] Ferguson D. Interactions between spacecraft and their environments. In: 31st Aerospace Sciences Meeting. USA: Proc. of AIAA; 1993. p. 705. DOI: 10.2514/6.1993-705

[35] de Groh K, Banks B, Hammerstrom A, Youngstrom E, Kaminski C, Marx L, et al. MISSE PEACE polymers: An international space station environmental exposure experiment. USA: Proc. AIAA Conf. on Intl. Space Station Utilizatio; 2001. Available from: http://gltrs.grc.nasa. gov/GLTRS

[36] Zhao X, Shen Z, Xing Y, Ma S. A study of the reaction characteristics and mechanism of Kapton in a plasma-type ground-based atomic oxygen effects simulation facility. Journal of Physics D: Applied Physics. 2001;**34**(15):2308. DOI: 10.1088/0022-3727/34/15/310

[37] Tagawa M, Matsushita M, Umeno M. Proceeding of the Sixth International Symposium on Materials in a Space Environment ESTEC; 19–23 September 1994; Noordwijk, The Netherlands, USA: Proc. of AIAA; pp. 189-193

[38] Milintchouk A, Van Eesbeek M, Levadou F, Harper T. Influence of X-ray solar flare radiation on degradation of teflon-laquo; in space. Journal of Spacecraft and Rockets. 1997;**34**(4): 542-548. DOI: 10.2514/2.3244

[39] Hall D, Fote A. 10 year performance of thermal control coatings at geosynchronous altitude. In: 26th Thermophysics ConferenceUSA: Proc. of AIAA; 1991. p. 1325. DOI: 10.2514/6.1991-1325

[40] Townsend J, Hansen P, Dever J, de Groh K, Banks B, Wang L, et al. Hubble space telescope metallized teflon (R) FEP thermal control materials: On-orbit degradation and post-retrieval analysis. High Performance Polymers. 1999; **11**(1):81-99. DOI: 10.1088/0954-0083/ 11/1/007

[41] Skurat VE, Nikiforov AP, Tenovoy AI. Proceedings of the Sixth International Symposium on Materials in a Space Environment ESTS; 19–23 September 1994; Noordwijk, The Netherlands: Proc. of AIAA; pp. 183-187

[42] Majeed R, More S, Phatangare A, Bhoraskar S, Mathe V, Bhoraskar V, et al. Synergetic effects of 1 MeV electron irradiation on the surface erosion in polyimide by atomic oxygen. Nuclear Instruments and Methods in Physics Research Section B: Beam Interactions with Materials and Atoms. 2021;**490**:49-54

[43] Arjun G, Lincy T, Sajitha T, Bhuvaneshwari S, Deepthi T, Devapal D. Atomic oxygen resistant polysiloxane coatings for low earth orbit space structures. Materials Science Forum. 2015;**830**:699-702

[44] Ferguson DC. Interactions between Spacecraft and their Environment. Cleveland, Ohio: NASA Lewis Research Center

[45] de Groh K, Banks B, Hammerstrom A. NASA/TM-2001-211311

[46] Koontz S, Albyn K, Leger L. Atomic oxygen testing with thermal atom systems—A critical evaluation. Journal of Spacecraft and Rockets. 1991;**28**(3): 315-323. DOI: 10.2514/3.26246

[47] Liu T, Sun Q, Meng J, Pan Z, Tang Y. Degradation modeling of

satellite thermal control coatings in a low earth orbit environment. Solar Energy. 2016;**139**:467-474

[48] Reddy M. Effect of low earth orbit atomic oxygen on spacecraft materials. Journal of Materials Science. 1995;**30**(2): 281-307

[49] Ferguson D. The energy dependence and surface morphology of kapton degradation under atomic oxygen bombardment. In: 13th Space Simulation Conference October. USA: Proc. of AIAA; 1984. p. 205

[50] Plis E, Engelhart D, Cooper R, Johnston W, Ferguson D, Hoffmann R. Review of radiation-induced effects in polyimide. Applied Sciences. 2019; **9**(10):1999

[51] Kuroda S, Terauchi K, Nogami K, Mita I. Degradation of aromatic polymers—I. Rates of crosslinking and chain scission during thermal degradation of several soluble aromatic polymers. European Polymer Journal. 1989;**25**(1):1-7. DOI: 10.1016/0014-3057 (89)90200-0

[52] Cherkashina N, Pavlenko V, Abrosimov V, Gavrish V, Trofimov V, Budnik S, et al. Effect of 10 MeV electron irradiation on polyimide composites for space systems. Acta Astronautica. 2021;**184**:59-69. DOI: 10.1016/j.actaastro.2021.03. 032

[53] Alegaonkar PS, Balaya P, Goyal PS, Bhoraskar VN. Dielectric properties of 1-MeV electron-irradiated polyimide. Applied Physics Letters. 2002;**80**:640. DOI: 10.1063/1.1435408

[54] Naddaf M, Balasubramanian C, Alegaonkar P, Bhoraskar V, Mandle A, Ganeshan V, et al. Surface interaction of polyimide with oxygen ECR plasma. Nuclear Instruments and Methods in Physics Research Section B: Beam Interactions with Materials and Atoms.

2004;**222**(1-2):135-144. DOI: 10.1016/j. nimb.2003.12.087

[55] Abdul Majeed R, Purohit V, Bhoraskar S, Mandale A, Bhoraskar V. Irradiation effects of 12 eV oxygen ions on polyimide and fluorinated ethylene propylene. Radiation Effects & Defects in Solids. 2006;**161**(8):495-503. DOI: 10.1080/10420150600810224

[56] Dokhale P, Bhoraskar V, Vijayaraghavan P. A study on boron diffusion in high density polyethylene using the (n, α) reaction. Materials Science and Engineering: B. 1998;**57**(1): 1-8

[57] Grossman E, Gouzman I, Verker R. Debris/micrometeoroid impacts and synergistic effects on spacecraft materials. MRS Bulletin. 2010;**35**(1): 41-47. DOI: 10.1557/mrs2010.615

[58] Abdul Majeed RMA, Datar A, Bhoraskar SV, Alegaonkar PS, Bhoraskar VN. Dielectric constant and surface morphology of the elemental diffused polyimide. Journal of Physics D: Applied Physics. 2006;**39**:4855-4859. DOI: 10.1088/0022-3727/39/22/017

[59] Vieth WR. Diffusion in and Through Polymers: Principles and Applications. Vol. 81. United States: American Scientist; 1991. p. 1

[60] Claeyssens F, Fuge G, Allan N, May P, Ashfold M. Phosphorus carbides: Theory and experiment. Dalton Transactions. 2004;**19**:3085-3092. DOI: 10.1039/B402740J

[61] Zhang R, Wang Z, Yu Y. Analysis of pm-526 inorganic paint by x-ray photoelectron spectroscopy. Chinese Journal of Materials Research. 1990; **4**(2):174-178

[62] Masui T, Hirai H, Hamada R, Imanaka N, Adachi GY, Sakata T, et al. Synthesis and characterization of cerium oxide nanoparticles coated with

turbostratic boron nitride. Journal of Materials Chemistry. 2003;**13**(3): 622-627. DOI: 10.1039/B208109A

[63] Böttcher CJF, Bordewijk P. Theory of Electric Polarization. Vol. 2. Amsterdam, EU: Elsevier Science Limited; p. 1978

[64] Mathakari N, Bhoraskar VN, Dhole SD. 6 MeV pulsed electron beam induced surface and structural changes in polyimide. Materials Science and Engineering B. 2010;**168**:122-126. DOI: 10.1016/j.mseb.2009.11.005

[65] Wilson D, Stenzenzenberger H, Hergenrother P. Polyimides. Glasgow and London: Blackie & Son; 1990

[66] Severin D, Ensinger W, Neumann R, Trautmann C, Walter G, Alig I, et al. Degradation of polyimide under irradiation with swift heavy ions. Nuclear Instruments and Methods in Physics Research Section B: Beam Interactions with Materials and Atoms. 2005;**236**(1-4):456-460. DOI: 10.1016/j. nimb.2005.04.019

[67] Nuclear Instruments and Methods in Physics Research Section B: Beam Interactions with Materials and Atoms. 2005;**236**:1-4, 456-460. DOI: 10.1016/j. nimb.2003.12.051

[68] Cho S, Jun H. Surface hardening of poly (methyl methacrylate) by electron irradiation. Nuclear Instruments and Methods in Physics Research Section B: Beam Interactions with Materials and Atoms. 2005;**237**(3-4):525-532. DOI: 10.1016/j.nimb.2005.03.007

[69] Uelzen T, Müller J. Wettability enhancement by rough surfaces generated by thin film technology. Thin Solid Films. 2003;**434**(1-2):311-315. DOI: 10.1016/S0040-6090(03)00484-X

[70] Vancso G, Hillborg H, Schönherr H. Chemical composition of polymer surfaces imaged by atomic force microscopyand complementary approaches. Polymer Analysis Polymer Theory. 2005;**35**:55-129. DOI: 10.1007/ 12_046

[71] Flitsch R, Shih D. A study of modified polyimide surfaces as related to adhesion. Journal of Vacuum Science & Technology A: Vacuum, Surfaces, and Films. 1990;**8**(3):2376-2381. DOI: 10.1116/1.576701

[72] Zhang Y, Yang G, Kang E, Neoh K, Huang W, Huan A, et al. Deposition of fluoropolymer films on Si (100) surfaces by Rf magnetron sputtering of poly (tetrafluoroethylene). Langmuir. 2002;**18**(16):6373-6380. DOI: 10.1021/ la011606j

[73] Shi M, Selmani A, Martinu L, Sacher E, Wertheimer M, Yelon A. Fluoropolymer surface modification for enhanced evaporated metal adhesion. Journal of Adhesion Science and Technology. 1994;**8**(10):1129-1141. DOI: 10.1163/156856194X00988

[74] Huslage J, Rager T, Schnyder B, Tsukada A. Radiation-grafted membrane/electrode assemblies with improved interface. Electrochimica Acta. 2002;**48**(3):247-254. DOI: 10.1016/S0013-4686(02)00621-7

[75] Ryan M, Fonseca J, Tasker S, Badyal J. Plasma polymerization of sputtered poly (tetrafluoroethylene). The Journal of Physical Chemistry. 1995; **99**(18):7060-7064. DOI: 10.1021/ j100018a044

[76] Rasoul F, Hill D, George G, O'Donnell J. A study of a simulated low earth environment on the degradation of FEP polymer. Polymers for Advanced Technologies. 1998;**9**(1):24-30. DOI: 10.1002/(SICI)1099-1581(199801)9:1< 24::AID-PAT730>3.0.CO;2-5

[77] Alegaonkar P, Bhoraskar V. Effect of MeV electron irradiation on the free volume of polyimide. Radiation Effects

and Defects in Solids. 2004;**159**(8-9): 511-516

[78] Stelmashuk V, Biederman H, Slavinska D, Zemek J, Trchova M. Plasma polymer films rf sputtered from PTFE under various argon pressures. Vacuum. 2005;**77**(2):131-137. DOI: 10.1021/ma0357164 10.1016/j. vacuum.2004.08.011

[79] Vasilets V, Shandryuk G, Savenkov G, Shatalova A, Bondarenko G, Talroze R, et al. Liquid crystal polymer brush with hydrogen bonds: Structure and orientation behavior. Macromolecules. 2004;**37**(10): 3685-3688. DOI: 10.1021/ma0357164

[80] Williams DH. Fleming. Spectroscopic Methods in Organic Chemistry. 2004

[81] Datar A, Bhoraskar SV, Bhoraskar VN. Surface modification of polymers by atomic oxygen using ECR plasma. Nuclear Instruments and Methods in Physics Research Section B: Beam Interactions with Materials and Atoms. 2007;**258**(2):345-351. DOI: 10.1016/j.nimb.2007.01.230

[82] Sun Y, Zhu Z, Li C. Correlation between the structure modification and conductivity of 3 MeV Si ion-irradiated polyimide. Nuclear Instruments and Methods in Physics Research Section B: Beam Interactions with Materials and Atoms. 2002;**191**(1-4):805-809. DOI: 10.1016/S0168-583X(02)00657-2

[83] Sun Y, Zhang C, Zhu Z, Wang Z, Jin Y, Liu J, et al. The thermal-spike model description of the ion-irradiated polyimide. Nuclear Instruments and Methods in Physics Research Section B: Beam Interactions with Materials and Atoms. 2004;**218**:318-322. DOI: 10.1016/ j.nimb.2003.12.051

[84] Vacík J, Červená J, Hnatowicz V, Pošta S, Fink D, Klett R, et al. Simple technique for characterization of ion-modified polymeric foils. Surface and Coatings Technology. 2000;**123**(2-3): 97-100. 10.1016/S0257-8972(99) 00515-0

[85] Stolterfoht N, Fink D, Petrov A, Muller M, Vacik J, Cervena J, et al. Characterization of etched tracks and nanotubules by ion transmission spectrometry. In: Proceedings. 3rd Annual Siberian Russian Workshop on Electron Devices and Materials. Vol. 1. Belarus, Russia: IEEE; 2002. p. 4. DOI: 10.1109/SREDM.2002.1024302

[86] From Solution F. Chemical deposition of chalcogenide thin films from solution. Advances in Electrochemical Science and Engineering. 2008;**12**:165. DOI: 10.1002/9783527616800

[87] Fink D, Alegaonkar PS, Petrov AV, Berdinsky AS, Rao V, Müller M, et al. The emergence of new ion tract applications. Radiation measurements. 2003;**36**(1-6):605-609

[88] Vacik J, Červená J, Hnatowicz V, Fink D, Kobayashi Y, Hirata K, et al. Study of latent and etched tracks by a charged particle transmission technique. Radiation Measurements. 1999;**31**(1-6): 81-84. DOI: 10.1016/S1350-4487(99) 00091-8

[89] Fink D, Klett R. Latent ion tracks in polymers for future use in nanoelectronics: An overview of the present state-of-the-art. Brazilian Journal of Physics. 1995;**25**:1

[90] Herden V. Das Verhalten von lichtinduzierten Ladungsträgern in Polysilane nunterbesonderer Berücksichtigung von Dotierung und strahlenchemischerVernetzung. na. 2001

[91] Krauser J, Weidinger A, Zollondz J, Schultrich B, Hofsäss H, Ronning B. Conducting ion tracks for field emission. In: Proc. Workshop on the

European Network on Ion Track Technology, Caen, France. 2002. pp. 24-26

[92] Lincot D, Froment M, Cachet H. Chemical deposition of chalcogenide thin dlms from solution. Advances in Electrochemical Science and Engineering. 1999;**6**:167-235

[93] Granström M, Berggren M, Inganäs O. Micrometer-and nanometer-sized polymeric light-emitting diodes. Science. 1995;**267**(5203):1479-1481. DOI: 10.1126/science.267.5203.1479

[94] Martin C, Nishizawa M, Jirage K, Kang M, Lee S. Controlling ion-transport selectivity in gold nanotubule membranes. Advanced Materials. 2001;**13**(18):1351-1362. DOI: 10.1002/1521-4095(200109)13:18<1351::AID-ADMA1351>3.0.CO;2-W

[95] Shtanko N, Lequieu W, Du Prez F, Goethals E. Preparation and properties of thermo responsive track membranes. In: Proceedings of the Workshop on European Network on Ion Track Technology. France: Caen; 2002

[96] Desai TA. Nanoporous microfabricated membranes: From diagnostics to drug delivery. In: Proceedings of MRS Fall Meeting. Boston. Germany: Wiley VCH; 27.11.2001–1.12.2001; ContributionY5.5. 2001

[97] Nishizawa M, Mukai K, Kuwabata S, Martin C, Yoneyama H. Template synthesis of polypyrrole-coated spinel $LiMn_2O_4$ nanotubules and their properties as cathode active materials for lithium batteries. Journal of the Electrochemical Society;**144**: 1923-1926

[98] Berdinsky A, Fink D, Muller M, Petrov A, Chadderton LT, Apel P Yu. Formation and conductive properties of miniaturized fullerite sensors. Proceedings of MRS Fall Meeting, Boston 27.11.2001–1.12.2001; Contribution Y4.7 2001.

[99] Chakarvarti S, Vetter J. Template synthesis—A membrane based technology for generation of nano-/micro materials: A review. Radiation Measurements. 1998;**29**(2):149-159. DOI: 10.1016/S1350-4487(98)00009-2

[100] Biswas A, Avasthi D, Singh B, Lotha S, Singh J, Fink D, et al. Resonant electron tunneling in single quantum well heterostructure junction of electrodeposited metal semiconductor nanostructures using nuclear track filters. Nuclear Instruments and Methods in Physics Research Section B: Beam Interactions with Materials and Atoms. 1999;**151**(1-4):84-88. DOI: 10.1016/S0168-583X(99)00086-5

[101] Klein J, Herrick R, Palmer D, Sailor M, Brumlik C, Martin C. Electrochemical fabrication of cadmium chalcogenide microdiode arrays. Chemistry of Materials. 1993;**5**:902-904. DOI: 10.1021/cm00031a002

[102] Liu K, Nagodawithana K, Searson P, Chien C. Perpendicular giant magnetoresistance of multilayered Co/Cu nanowires. Physical Review B. 1995;**51**(11):7381. DOI: 10.1103/PhysRevB.51.7381

[103] Hjort K. The European network on ion track technology. In: Proceedings of the Fifth International Symposium on "Swift Heavy Ions in Matter". Sweden: DiVA; May 22–25, 2002; Giordano Naxos, Italy. 2002